EVALUATION OF F-18 LABELED HYDROXY QUINOLINE DERIVATIVE AS A POTENTIAL PET IMAGING AGENT FOR EARLY DETECTION OF ALZHEIMER'S DISEASE

APPROVED BY SUPERVISORY COMMITTEE

Padmakar Kulkarni, Ph.D., Mentor

Frederick J. Bonte, M.D., Chairman

Nikolai Slavine, Ph.D.

Bao-Xi Qu, M.D.

EVALUATION OF F-18 LABELED HYDROXY QUINOLINE DERIVATIVE AS A POTENTIAL PET IMAGING AGENT FOR EARLY DETECTION OF ALZHEIMER'S DISEASE

by

Mustafa Alhasan

DISSERTATION

Presented to the Faculty of the Graduate School of Biomedical Sciences

The University of Texas Southwestern Medical Center at Dallas

In Partial Fulfillment of the Requirements

For the Degree of

DOCTOR OF PHILOSOPHY

The University of Texas Southwestern Medical Center at Dallas

Dallas, Texas

November, 2011

Acknowledgments

I would like to thank my committee members who guided and supported me to finish my graduate project. I also would like to thank my colleagues in the program who shared with me the great times I spent in the University of Texas Southwestern. I would like to thank Dr. Antich for supporting and accepting me in the program. Thanks to Dr. Kulkarni for his supervision and guidance during my study. Special thanks to Dr. Bonte for sharing his great knowledge in Alzheimer's disease with me. In addition, thanks to Dr. Slavine for image processing and analysis, and Dr. QU for teaching me the histological procedures I used during my study.

Thanks to Dr. Veera, Dr. Srinivas and Lakshman for helping me conduct the chemistry experiments in my study, and Dr. Sun's laboratory group for teaching me the PET/CT techniques. In addition, I would like to thank Dr. Mason and his laboratory group for training me in the multi-modality imaging including optical and ultrasound imaging, and Dr. Lewis for teaching me ultrasound and fluorescence imaging techniques. Thanks to Kay Emerson and Dr. Ravnik for their support. I would like to thank Jordan University of Science and Technology (JUST) for the financial assistance I received during my study.

Finally, I would like to dedicate this work to my family: my deceased father, my mother, and sisters for supporting and helping me to achieve my dreams.

EVALUATION OF F-18 LABELED HYDROXY QUINOLINE DERIVATIVE AS A POTENTIAL PET IMAGING AGENT FOR EARLY DETECTION OF ALZHEIMER'S DISEASE

Mustafa Alhasan, Ph.D.

The University of Texas Southwestern Medical Center at Dallas, 2011

Padmakar Kulkarni, Ph.D.

Alzheimer's disease (AD) is a neurodegenerative disorder characterized by a progressive cognitive decline in the elderly people older than 65 years of age. The pathological hallmarks of the disease include extracellular senile plaques and intracellular tangles developing during the pre-symptomatic stage. Although the definite diagnosis of AD is only possible post-mortem, non-invasive imaging has

provided an important tool for early detection, and has helped in planning for an effective treatment. Targeted molecular imaging using positron emission tomography (PET) has provided the insight into understanding different disease mechanisms with high sensitivity. Based on the amyloid cascade hypothesis, congo red and thioflavine derivatives have been investigated as potential PET ligands that bind specifically to the amyloid plaques. Another hypothesis, the metal hypothesis, suggested that elevated level of metals particularly zinc, copper and iron, can interact with amyloid beta proteins to form metal complexes. The use of metal chelation therapy has emphasized the involvement of metals in the aggregation of plaques and has shown promising results in clinical and animal studies through dissolving plaques and restoring the metals balance in the affected brains. In this study, based on the metal hypothesis, ^{18}F-labeled 8-hydroxy quinoline was investigated as a potential PET imaging agent for early detection of AD in APP/PS1 mouse model. This agent demonstrated high binding affinity to the plaque aggregates (1.5 nM), and increased fluorescence intensity upon binding to zinc. In addition, *in vivo* studies showed the feasibility of differentiating mice with AD from normal control mice ($p < 0.05$), and the ability to detect different plaque densities at different ages of AD (4, 6, and 12 months). Good correlations were found between autoradiography, histology and PET images. The biodistribution data demonstrated rapid uptake and clearance of this compound in the normal brain of wild-type mice.

Table of contents

List of Figures

List of Tables

List of Appendices

List of abbreviations

AD	Alzheimer's disease
Aβ	Amyloid beta
NFTs	Neurofibrillary tangles
PSEN	Presenilin
APP	Amyloid precursor protein
MCI	Mild cognitive impairment
SP	Senile plaque
KPI	Kunitz protease inhibitor
CAA	Cerebral amyloid angiopathy
MAP	Microtubule associated protein
APOE	Apolipoprotein E
ABSENT	Amyloid Beta Synergistic Endothelial and neuronal toxicity
ZnT	Zinc transporter
MT	Metallothionein
GIF	Growth inhibitor factor
CSF	Cerebrospinal fluid
MRI	Magnetic resonance imaging
CT	Computed tomography
PET	Positron emission tomography
SPECT	Single photon emission tomography
DTI	Diffusion tensor imaging
BOLD	Blood oxygen level dependent
PIB	Pittsburgh Compound-B
OB	Olfactory bulb
CX	Cerebral cortex
HC	Hippocampus
CB	Cerebellum
SUV	Standardized uptake value
ID	Injected dose
TACs	Time activity curves
AUC	Area under curve
ROI	Region of interest
HQ	Hydroxy quinoline
CPM	Counts per minute
DLU	Digital light unit
FI	Fluorescence intensity
S value	Mean dose per unit cumulated activity

1. Introduction

1.1. History of Alzheimer's disease

In 1907, Alois Alzheimer described a case of a 51-year old woman who presented with symptoms of progressive memory loss and psychological disturbances that could not be attributed to a recognized disease. The patient died four years after the onset of her illness. Postmortem examination showed brain atrophy and disintegration of cortical neurons identified by the presence of neurofibrillary tangles and amyloid plaques (1).

This new histological finding and the unusual early onset of the illness represented a unique type of dementia. Initially, Alzheimer's disease (AD) was described as pre-senile dementia for patients younger than 65 years of age, and senile dementia of Alzheimer type for patients older than 65 years. However, AD has become a single disease, mostly occurring in people older than 65 years of age (2).

1.2. Alzheimer's disease characteristics

Alzheimer's disease is the most common cause of dementia. It represents an immuno-inflammatory reaction resulting in the activation of the immune system in response to aberrant proteins located in the brain and leading to neurotoxicity (3). The abnormal function of these intracellular and extracellular proteins results in death of neurons (4). Neurodegenerative disorders are defined as progressive loss of neurons. The most common types

of neurodegenerative disorders causing dementia include Alzheimer disease, Parkinson's disease, fronto-temporal dementia and dementia with Lewy bodies. Every one of these diseases has a unique pathogenesis. The pathologic hallmarks of AD are extracellular beta amyloid (Aβ) plaques and intracellular neurofibrillary tangles (NFTs) (5). In addition, AD results in brain atrophy and synaptic loss leading to cognitive decline (6). Other common symptoms of AD include hallucinations, confusion, language problems, seizures and incontinence. Pneumonia and other infections can result in death (8).

Cases of AD are classified into familial and sporadic. In contrast to the late-onset sporadic type, the familial type is characterized by early onset and associated with clinical manifestations such as aphasia, psychiatric disturbance and seizures. Whether these signs are related to the early onset of the disease or its mechanism is still unknown. However, both types have common pathologic features in terms of the presence of neuronal loss, amyloid plaques and the tangles (7). Familial AD accounts for only 25% of all AD cases. There are three types of gene mutation associated with the familial AD including presenilin (PSEN 1-2) and amyloid precursor protein gene (APP). PSEN1 gene mutation accounts for most cases of familial AD while APOE4 mutation is more common in the late-onset type of AD (8, 9).

People with Down's syndrome are thought to develop AD since they have over expression of APP gene in chromosome 21, resulting in an

increased cleavage of APP into Aβ1-40 and Aβ1-42 and subsequently forming plaque aggregates (10). Half of patients over 50 years of age with Down's syndrome are at risk of developing AD (11).

Mild cognitive impairment (MCI) represents a transitional state between normal aging and AD. It is defined as a cognitive decline without affecting daily functions. Half of people with MCI are expected to develop dementia within 5 years. Controlling the risk factors such as hypertension during this stage may prevent the development of AD (12, 13, 14).

1.3. Epidemiology

Currently, 5.3 million Americans are suffering from AD. Affected individuals aged 65 years and older account for 5.1 million while only 200,000 individuals are under the age of 65 years (15). The number is estimated to reach 16 million by 2050. Worldwide, people with dementia mostly from AD are about 35 million and expected to be 115 million by 2050 (16). The prevalence of AD in people aged 71 years and older is about 14%; women have higher rate of developing AD (16%) than men (11%) possibly due to higher living expectancy (15, 17, 18). The incidence rate of AD showed increased number of the new cases from 411,000 cases in 2000 to 454,000 cases in 2010, and is estimated to be 959,000 cases by 2050 (15, 19). This can be due to the increase in the population aged 85 years and older (currently 5.5 million and 19 million is estimated in 2050).

AD was ranked as the seventh leading cause of death in all patients and the fifth for people aged 65 years of and older in 2006. The mortality rate due to AD has increased by 46% between 2000 and 2006 while that of other leading causes of death such as stroke and cancer declined. The mortality of AD patients aged 75-84 is 2.5-fold higher than patients aged 55-74, and the mortality of patients aged 85 years and older is 2-fold higher than patients aged 75-84 (15). The median survival of women and men after initial diagnosis is 5.7 and 4.2 years, respectively (20).

1.4. Amyloid plaques

Senile plaques (SP) are spherical extracellular lesions measuring 10-150 μm in diameter initially detected using Bielschowsky silver technique. Many types of SP have been identified including diffuse, primitive, neuritic and compact plaques. Clinically, diffuse and neuritic plaques are considered the most frequent types of plaques detected in neuropathologic examinations (21). They are mostly localized in the hippocampus, the amygdaloid nucleus and the cerebral cortex regions. Diffuse plaques are irregular shapes of non-fibrillar Aβ deposits. Primitive plaques is composed of altered neurites but lack amyloid core while classic plaques are characterized by the presence of both amyloid core and altered neurites. Amyloid core without altered neurites was found in the compact plaques. Neuritc, classic and compact plaques are mature plaques composed of fibrillar Aβ deposits (22, 23). Interestingly,

Amyloid deposition can occur in the cerebellar cortex and may represent an intermediate type between the diffuse and the compact deposits (24). In addition, senile plaques are surrounded by microglial cells reflecting the key role of these cells in the formation of the plaques (25, 28). Amyliod plaques are composed of small peptides (Aβ) resulting from the cleavage of β-amyloid precursor protein (APP) which is encoded by a gene located in chromosome 21 (36).

The amyloid precursor protein (APP) can be found in different forms including APP770, APP751 and APP695. APP695 protein is abundant in the neurons while APP770 and APP751, expressing a serine protease inhibitory domain called Kunitz protease inhibitor (KPI), are mostly found in the glial cells. It has been reported that the shift of APP695 to APP-KPI in neurons can result in higher production of Aβ deposits in the brain (37). The function of APP was linked to different processes including neurite outgrowth, protein transport along the axon, calcium metabolism and transmembrane signal transduction (38). The cleavage of APP by α-secretase results in sβAPP$_{\alpha}$ amino terminal fragment and prevents the formation of Aβ. In addition, β-secretase cleaves APP and leads to the formation of sβAPP$_{\beta}$ and amyloidgenic carboxyl terminal fragment, which is eventually cleaved by γ-secretase to yield Aβ peptide (39).

Moreover, as Aβ deposits were identified in the brain tissues in the form of SP, they were found to accumulate in the cerebral vessels. The deposition of these congophilic substances in the walls of cerebral arteries, arterioles, capillaries and veins is called cerebral amyloid angiopathy (CAA). This pathologic finding was reported in more than 70% of AD patients (26). The deposition of Aβ within the walls of the vessels can lead to fragility, rupture and eventually intracerebral hemorrhage. Age is the most common risk factor for CAA, and similar to AD, the occurrence of sporadic type CAA is more common than the familial type (27).

1.5. Neurofibrillary tangles

Neurofibrillary tangles (NFTs) are characterized by abnormal accumulation of a congophilic filament substance in the neuritc processes of the hippocampus and the cortex. Dementia was found to correlate with the number of NFTs and neuronal loss. Other forms of dementia such as dementia of Parkinson's disease and Down's syndrome were reported to have the same type of lesion (29). The initial formation of NFTs in the cortex affects pyramidal cells in the transentorhinal region followed by the limbic system. Subsequently, the process continues to cover the temporal, frontal and occipital areas (31).

The structure of NFTs was first identified by electron microscopy as a paired of helical filaments (30). The main component of the NFTs was found

to be the microtubule-associated protein (tau) identified by using anti-tau sera (32). Tau protein is a member of the microtubule associated protein (MAP) family and is responsible for stabilizing the microtubules. It is one of the smallest proteins in this family (<200 KDa) (33). Hyperphosphorylation of the protein destabilizes the microtubule and leads to protein transport failure and neuronal toxicity. The gene which encodes the tau protein is found in chromosome 17q21 and consists of 16 exons (34, 35).

1.6. Amyloid Hypothesis

Amyloid β protein was first identified and reported as a marker for AD in the 1980's, after isolation from β-pleated sheet fibrils located in the cerebrovascular amyloidosis of an AD case. This was based on the fact that more than 90% of AD patients suffer from CAA. In addition, the amino acids sequence of the cerebrovascular amyloid protein isolated from a case of Down's syndrome was found to be homologous to the Amyloid β protein found in the AD case (40, 41). This discovery led researchers to investigate the role of amyloid deposits in AD pathogenesis. Moreover, studies have shown that mutation of the gene encoding Amyloid β (APP gene) in chromosome 21 is one cause of AD (42). Mutant APP was found to yield 5-fold more amyloid beta protein than the wild type gene. This suggests that mutation of APP tends to increase the amount of Amyloid β protein through β and γ secretases pathways (43).

The amyloid cascade hypothesis was first proposed in 1991 by John Hardy. In this hypothesis, APP is cleaved at residues 15 to 17 by secretase to produce fragments that lack intact Aβ protein and eventually no amyloid deposition occurs. The other pathway is processed by lysosomes which results in carboxyl-terminal fragments containing the entire Aβ protein and causing amyloid deposition (44). These deposits are toxic and will eventually result in the formation of NFTs and death of neurons. The formation of NFTs is suggested to be the consequence of increased calcium ions concentration inside the neurons leading to hyperphosphrelation of tau protein (44). In addition, presenilin 1 and presenilin 2 mutations were shown to increase the concentration of the extracellular Aβ *in vivo* (45).

Four reasons were reported to support the amyloid hypothesis. First, in most cases of tau protein mutations which cause the formation of the NFTs in the frontotemporal dementia, the mutation is not sufficient to produce amyloid plaque deposits as in AD. This suggests that the formation of the NFTs occurs after the deposition of the plaques in AD patients. Second, transgenic mice expressing both APP and tau have shown increased production of NFTs in comparison to tau protein alone. This confirms that the presence of plaques increased the formation of NFTs. Third, APOE 4, which is responsible for most cases of late-onset AD, has shown to be involved in the metabolic pathway of the plaque formation when crossed with APP mice. Finally,

imbalance between the catabolism and the clearance of the plaques is a risk factor for developing late-onset AD (46).

Although the amyloid cascade hypothesis has been supported for a long time, many limitations have been reported. Aβ plaques were not found to be neurotoxic *in vivo*. Plaques density doesn't correlate with the severity of dementia, because many non-demented elderly people have the same density of plaques as in AD patients. In addition, Aβ plaques density doesn't correlate with the neuronal and synaptic loss, and vaccination of impaired memory transgenic mice expressing APP/PS1 against the plaques, didn't improve the cognition function (47).

1.7. Amyloid Beta Synergistic Endothelial and neuronal toxicity (ABSENT) hypothesis

Since the amyloid hypothesis couldn't explain many aspects of the mechanism underlying the progression of AD, another hypothesis combining amyloid plaques and vascular dysfunction has been proposed. This hypothesis is known as amyloid beta synergistic endothelial and neuronal toxicity (ABSENT) (48). It suggests that Aβ deposits induce vascular dysfunction and neuronal damage by increasing the level of free radicals. During MCI stage, a low level of Aβ can induce indirect neurotoxicity via vascular dysfunction. In the middle and the late stages of AD, the high density of plaque deposits can directly induce neurons death. In addition, the toxicity of Aβ to the endothelial

cells of the vessels is mainly due to high superoxide radical production, while the neurotoxicity is due to the high level of lipid-soluble free radicals. Both radicals are produced from the Cu-β cycling. Normally, radicals are detoxified by antioxidants like glutathione and catalases. However, in AD patients, increased concentration of Cu-β molecules will cause overwhelming of the normal detoxification mechanism, since the number of the antioxidants is not sufficient to overcome the detoxification (48).

1.8. Metal Hypothesis

The most recent hypothesis of AD pathogenesis has proposed that the toxicity and the deposition of Aβ in specific regions of the brain are due to the interaction with metals particularly zinc and copper (49). There are many reasons for proposing this hypothesis. First, soluble Aβ are present in normal brain, which means that the toxicity of Aβ could be mediated by other factors. Second, the deposition of plaques is usually focal rather than being uniformly distributed in AD patients. Third, increased Aβ accumulation doesn't correlate well with age implying that metal mediated oxidative damage plays an important role in AD pathology (49).

Zinc and copper were found to precipitate and aggregate plaques. Copper can cause aggregation of plaques under acidic pH condition (6.8-7), which was reported in many inflammatory diseases (49, 50, 51). It was noticed that in rats and mice, Aβ have a special amino acid sequence that

decreases the binding to metals. This may explain why these animals have less chance in developing plaque deposits (49).

There are two binding sites of Aβ with high and low affinity to the metals. Low affinity binding with zinc has been shown to precipitate the plaques and reduce the cleavage by α secratase. In addition, copper was shown to have a higher affinity for Aβ42 than Aβ40 (49). APOE4 which is responsible for the late-onset cases of AD was found to increase the aggregation of plaques mediated by copper and zinc *in vitro*. This might suggest that APOE4 is involved in the plaques aggregation (52). Upon binding to metals and formation of amyloid metal complex, Aβ reduces these metals and produces H_2O_2 and free radicals. This reduction is partially induced by tyrosine (53) and other reducing agents such as cholesterol (54). In addition to H_2O_2, toxic lipid products can be produced, which have been found to be at high level in AD patients. H_2O_2 was reported to be highly associated with Aβ42 in comparison to Aβ40, and this corresponds to the fact that Aβ42 is more likely to be the major component of the amyloid plaques (55).

Zinc, copper and iron are found in normal tissues. However, the concentrations of these metals in the AD brain were found at much higher level (copper: 390μM, zinc: 1055μM, iron: 940μM) in comparison to normal control individuals (49, 56). These metals are not usually present as free; they are usually bound to ligands such as transferrin. On the other hand, free

release of zinc and copper metals was reported in the glutamatergic synpases in the cortex and the hippocampus (57). Interestingly, ZnT3 which regulates the concentration of zinc is found exclusively in the membrane of the glutamatergic vesicles (49). In addition, NMDA activation in the neurites can release free copper (58). Free metals then bind to Aβ in the synaptic cleft to form the metal complex and produce free radicals. This reaction can be prevented by the presence of Metallothionein-3 (MT3), which is released from the astrocytes. However, MT3 level or the growth inhibitor factor (GIF) is decreased in AD patients (59), and this might be the cause of increasing the possibility of Aβ metal complex formation. This hypothesis suggests the use of chelating agents to target the reaction between metals and Aβ to reduce the formation of Aβ aggregates (49).

1.9. Metal chelators as therapeutic agents

Based on the metal hypothesis and the proposed mechanism of blocking metal-amyloid protein interactions, metal chelators have been investigated as potential therapy for AD through reducing the neurotoxicity and restoring the metals homeostasis in the brain (49). Trivalent ion chelator, desferrioxamine was the first chelating agent used for treating AD patients. The results suggested rapid reduction of the decline in daily living skills (60, 61). In addition, the lipophilic metal chelator DP-109 (1,2-bis(2-aminophenyloxy) ethane-*N*,*N*,*N*′,*N*′-tetraacetic acid, *N*,*N*′-bis(2-

octadecyloxyethyl)ester, *N*,*N*′-disodium salt) was investigated in female hAbetaPP-transgenic Tg2576 mice and was found to reduce the burden of amyloid plaques and cerebral amyloid angiopathy. This theory suggests that metals are involved in the deposition of aggregated plaques in AD (62).

Another bifunctional chelating agent, XH1 (([(4-benzothiazol-2-yl-phenylcarbamoyl)-methyl]-{2-[(2-{[(4-benzothiazol-2-yl-phenylcarbamoyl)methyl]-carboxymethyl-amino}-ethyl)-carboxymethyl-amino]-ethyl}-amino)-acetic acid) which has amyloid binding and metal chelating moieties, has been examined in APP/PS1 transgenic mice and showed attenuation of the plaques without inducing noticeable toxicity (63). Treating APP2576 transgenic mice with clioquinol resulted in 49% decrease in brain Aβ deposition and an increase of soluble Aβ (1.45%). It also suggests that targeting the interactions of Cu and Zn with Aβ can help in the prevention and the treatment of AD (64). In addition, Clioquinol in phase 2 clinical trials showed reduced level of amyloid beta protein in the plasma and an elevated level of plasma zinc of treated AD patients in comparison to controls, suggesting a promising therapeutic approach for AD (65).

The results of metal chelation therapy provided great evidence about the involvement of different metals particularly zinc, copper and iron in the aggregation of the amyloid plaques. Disruption of metal amyloid beta interactions can help in dissolving the aggregates and restoring the balance of

the metal ions. However, this treatment approach needs further evaluation in large number of patients in the clinical trials, to test the drug effect with other medications which may improve the AD treatment.

1.10. Animal models

There are many animal models that have been proposed to mimic the AD of human in order to understand the underlying mechanisms of the disease and to test the efficacy of different drugs to prevent and treat AD. Based on many reported pathophysiological processes associated with AD, such as hypofunction of the forebrain cholinergic system, aggregation of Aβ peptides, NTFs formation, brain inflammation, deficiency in the glucose metabolism and aging, rodents have been engineered to express such pathologies (66).

The association between hypofunction of the forebrain cholinergic system and the memory impairment was demonstrated in humans after treating normal subjects with Scopolamine. It induced memory and cognitive decline and upon treating with antagonist of Scopolamine, cognitive and memory functions were improved (67). It was reported that treatment with muscarinic receptor cholinergic agonist, can decrease the level of APP in the neocortex and the hippocampus in normal and forebrain cholinergic deficits rats. This high level of APP in the neocortex and the hippocampus of the tested rats showed late escape in water maze. This suggests that there is a link

between the level of APP, cholinergic function and the impairment of memory in AD patients (68).

This model is limited by the fact that the hypofunction of the forebrain cholinergic system doesn't contribute to the formation of Aβ plaques and NFTS as in AD (66). Aβ protein deposition has a major role in developing AD according to the Aβ cascade hypothesis. The injection of synthesized Aβ peptides into the septum of rat's brain showed a reduction in the hippocampal acetylcholine. This suggests the induced hypofunction of the hippocampal cholinergic system (69).

Disruption of object recognition was observed few weeks after the injection of Aβ peptides into the nucleus basalis of the rats followed by impaired performance 2 months later. This model demonstrated the role of the plaques in cognitive impairment as seen in AD (70). Hence, targeting Aβ peptides can reduce plaques deposition. *In vivo* treatment with β-sheet breaker peptide blocked the process of plaque deposition through stabilizing the normal structure of the peptide and destabilizing the β-sheet structure (71). Although the model of injecting Aβ peptides directly to the brain is promising for AD, the injected amount of the peptide is much higher than that found in AD cases (72).

To explore the familial AD type, transgenic mice expressing the most common gene mutations (APP, PS1, PS2, APOE) in AD have been generated.

APOE gene mutation which is responsible for late onset AD has been reported to play an important role in the deposition of Aβ plaques. This was demonstrated using transgenic mice over expressing human amyloid protein precursor (APP V717F+/-) with none, one and two alleles of *APOE*. The results showed no Aβ deposits in mice without APOE, while mice with one or two alleles of *APOE*, showed increased plaque deposition. In addition, the amount of the deposits was dose dependent; mice with two alleles of *APOE* showed higher amount than mice with single allele (73). Although this model represents a good way for investigating AD, none of the transgenic mice over expressing Aβ has shown the formation of NFTs which is a feature of AD, and there is no correlation between the density of the plaques and NFTs (74).

Neuroinflammation is another mechanism underlying the neurodegenerative diseases. Injection of β (1–40) amyloid peptide into the nucleus basalis of rats induced activation of the microglial cells around the plaque deposits (77). However, treatment with anti-inflammatory drugs such as prednisone showed no differences between control and treated AD patients in terms of cognitive decline (78).

Aging rodent is another model for AD investigation. However, they don't develop the same pathological markers of AD (66). A list of different transgenic mice, behavioral characteristics and the onset of Aβ formation are summarized in other reviews (75, 76).

1.11. Diagnosis criteria and biomarkers

The diagnosis of Alzheimer's disease is only definite at postmortem examination. The postmortem criteria for definite AD have been reported by Khachaturian in 1985. He suggested that AD diagnostic criteria should be based on the quantification of the plaques amount and correlated with different ages of AD patients. On the other hand, in 1991, Braak and Braak described another pattern to confirm AD through correlation with NFTs instead of plaques.

However, clinical examinations for early diagnosis of AD can be made by investigating the patient history, symptoms related to cognitive, social and occupational impairment. In addition, CT and MRI can rule out other causes of dementia such as tumors, hematoma and hydrocephalus. Measuring CSF biomarkers level such as Aβ42 and tau proteins has shown good accuracy to differentiate demented patients form normal matched age subjects, but with lower sensitivity for differentiating the AD type dementia from other types. In this test, lower level of Aβ42 and high level of hyperphosphorylated and total tau proteins were found in AD patients in comparison to controls. Moreover, decreased FDG uptake in specific brain regions including temporoparietal cortex has been used as a good biomarker for AD (2, 79, 80).

1.12. Imaging techniques

MR imaging

MRI has been used routinely in clinics to identify structural changes in normal brain and to rule out other pathological causes which might have the same effect as the neurodegenerative diseases. The hippocampus in the medial temporal lobe is one of the earliest affected regions in AD (31). In addition, diffuse brain atrophy was noticed in AD patients in comparison to controls as reduced gray matter volume in the frontal, temporal and occipital lobes (81).

For early detection of AD, particularly in the MCI stage, the application of MRI was limited to differentiate between MCI-converters and non-converters, where they showed heterogeneous results (82). Although MRI can show good structural changes, low and relatively high magnet fields (3 and 4 T) have limited resolution, and 7 T which currently in the clinical research can further improve the resolution (83). In addition, diffusion tensor imaging (DTI) MRI technique showed that the fractional anisotropy (FA) of the cingulum fibers was reduced in MCI patients and further reduced in AD patients. This technique improved the accuracy of AD diagnosis beside the structural changes of the hippocampus region (84).

Moreover, MR spectroscopy of neuronal marker N-acetylaspartate (NAA) showed reduced level of this metabolite in AD patients in comparison to controls, and increased the detection accuracy to 95% in comparison to the

hippocampus volume change detection (89%) alone (85). Functional MRI (fMRI) based on blood oxygen level dependent (BOLD) technique has been used to study the changes associated with blood volume and cerebral blood flow in neurodegenerative diseases. Using learning tasks during fMRI study to test the brain activation in AD and normal subjects, a reduction in brain activity was noticed in the medial temporal lobe memory system of AD patients in comparison to normal subjects (86).

Although MRI techniques have been promising for differentiating normal from AD subjects, early detection in the pre-symptomatic stage is crucial for treatment planning.

PET imaging

Targeting molecular pathologies such as amyloid plaques and tau proteins may improve the early detection of Alzheimer's disease. PET (Positron Emission Tomography) imaging ligands based on congo red and thioflavine derivatives such as Pittsburgh Compound-B (^{11}C-PIB) has shown the potential for specifically binding amyloid plaques in AD patients with higher retention than that in controls, and a good correlation with FDG PET (87). ^{18}F labeled agents such as ^{18}F-AV-45 are being developed as ^{18}F has longer half life (110 min VS. 20 min for ^{11}C) and more convenient for production and transportation (88). Although PIB and [^{18}F] FDDNP have

shown the potential for binding to plaques *in vitro*, they both failed to differentiate between control and AD mice *in vivo* imaging (89).

SPECT imaging

SPECT (Single Photon Emission Computed Tomography) imaging has been used to study dementia. ^{99m}Tc-HMPAO has shown the feasibility to differentiate between AD patients and control subjects (90). Moreover, regional cerebral blood flow (RCBF) using inhaled xenon-133 SPECT technique has been correlated with clinical and histopathologic diagnosis of AD and healthy subjects. Clinical diagnosis was correct in 15 of 18 patients (91).

Opazo et al. evaluated I-125 labeled clioquinol in control subjects and AD transgenic (Tg2576) mice and I-123 labeled CQ in humans (92). Their data showed slight elevation of the tracer brain uptake in AD mice (compared to control mice) at 15 min post injection of the tracer. However, it was <1% ID/g in both cases. Their data showed that the movement of the tracer into the human brain was similar to I-125 CQ brain distribution in mice. SPECT imaging studies in humans volunteers (healthy and mild AD) with I-123 CQ were not encouraging as the tracer signal was too low to permit imaging. Tracer counting was possible in the cerebral hemispheres although counts were not sufficiently high to achieve reliable data from other brain regions such as the cerebellum (92). Even though the brain uptake of CQ was too low

to permit reliable imaging studies, their findings established the principle of developing the class of compounds represented by CQ (quinolines) as potential Aβ ligands for *in vivo* imaging.

Compared to current amyloid-targeting imaging agents, the class of molecule represented by CQ interacts with an alternative, metal-associated, biochemical target, which may be useful in the differentiation of AD pathology. In comparison to SPECT, PET imaging showed higher sensitivity and specificity; 87-90% and 85-92%, respectively (93).

Optical imaging

Optical imaging has been used for animal research to detect amyloid plaques utilizing different fluorescence probes. Multi-photon microscopy provided a powerful tool for *in vivo* imaging of cells, beside the conventional fluorescence microscope. Fluorescence probes such as BSB ((*trans,trans*)-1-bromo- 2,5-bis-(3-hydroxycarbonyl-4-hydroxy)styrylbenzene)) and thioflavin-S have been reported to be specific dyes for amyloid plaques (94-99).

Combining structural, functional and targeted molecular imaging will improve the early detection of AD, and can longitudinally be used to monitor therapy outcomes. However, more studies are needed to evaluate the feasibility of combining such techniques in terms of cost, safety, and efficiency.

2. Synthesis and radiochemistry of 2-F-8-HQ

2.1 Background

Our previous studies showed that the uptake of I-125 CQ (clioquinol) in mice brains was low (~ 1 %). However, the uptake could be enhanced by encapsulating the tracer in burtylcyanoacrylate nanoparticles (100). Opazo et al. evaluated I-125 labeled clioquinol in control and AD transgenic (Tg2576) mice and I-123 labeled CQ in humans (92). Their data showed slight elevation of the tracer brain uptake in AD mice (compared to control mice) at 15 min post i.v. injection of the tracer.

However, it was <1% ID/g in both the cases. Their data showed that the movement of the tracer into the human brain was similar to I-125 CQ brain distribution in mice. SPECT imaging studies in humans volunteers (healthy and mild AD) with I-123 CQ were not encouraging as the tracer signal was too low to permit imaging. Tracer counting was possible in the cerebral hemispheres although counts were not sufficiently high to achieve reliable data from other brain regions such as the cerebellum (92).

Even though the brain uptake of CQ was too low to permit reliable imaging studies, their findings establish the principle of developing the class of compounds represented by CQ (quinolines) as potential Aβ ligands for *in vivo* imaging. Compared to current amyloid-targeting imaging agents, the class of molecule represented by CQ interacts with an alternative, metal

associated, biochemical target, which may be useful in the differentiation of AD pathology. Synthesis and evaluation of similar molecules including 2-F-8-HQ were investigated by Dr. Kulkarni (UT Southwestern) and Dr. Vasdev (University of Toronto) (101).

2.2. Materials and methodology

Synthesis of 8-(benzyloxy)-2-chloroquinoline (precursor for labeling)

8-Hydroxy-2-chloroquinoline, (TimTec LLC; 1.0 g, 5.6 mmol), was dissolved in DMF (10 mL) in a round bottom flask. Potassium carbonate (1.6 g, 11.4 mmol) was added into the flask followed by addition of benzyl chloride (1.3 mL, 11.4 mmol). The reaction mixture was stirred for 2 h at 60 ^{o}C. Completion of the reaction was monitored by thin layer chromatography (Hex/EtOAc/HOAC 89:9:2, v/v, R_f = 0.3). Upon completion, the reaction mixture was extracted with CH_2Cl_2 (3 × 50 mL) and the combined organic fractions were extracted with H_2O (2 × 50 mL) and brine (50 mL).

The organic layer was then dried (Na_2SO_4), filtered and concentrated to yield a light pink solid (1.33 g, 88.8%). Mp: 92 – 94 ^{o}C. ^{1}H NMR ($CDCl_3$, 300 MHz) δ (ppm): 7.94 (d, *J* = 8.6 Hz, 1H, ArH), 7.41 (d, *J* = 7.3 Hz, 2H, ArH), 7.31-7.17 (m, 6H, ArH), 6.96 (dd, *J* = 4.8 Hz, *J* = 2.0 Hz, 1H, ArH), 5.34 (s, 2H, -CH_2-). HRMS (EI) calculated for $C_{16}H_{12}ClNO$ (+): 269.0607 amu, observed: 269.0607 amu. Isotopic pattern for Cl (3:1) was observed (101).

Synthesis of 8-(benzyloxy)-2-fluoroquinoline (precursor for cold compound preparation)

8-benzyloxy-2-chloroquinoline (50 mg, 371 μmol) and 6 mL of 1 M tetra-n-butylammonium fluoride (TBAF) in tetrahydrofuran (THF solvent was removed by rotary evaporation prior to usage) were added into DMSO (20 mL) in a septum-sealed 20 mL glass tube (Biotage). The reaction mixture was heated to 140 ^{o}C in a microwave reactor (Biotage Initiator) and stirred for 1 h. Reaction progress was monitored to completion by HPLC [Luna Phenyl-Hexyl 150×4.6 mm; CH_3CN/H_2O (65:35 v/v) + 0.1 N ammonium formate (AF); flow rate of 1 mL/min; monitored by UV (λ= 254)] until 8-Hydroxy-2-chloroquinoline (t_R = 5.0 min) was consumed. Completion of the reaction was further confirmed by thin layer chromatography (Hex/EtOAc/HOAC 89:9:2, v/v, R_f = 0.5).

The reaction mixture was then diluted with 100 mL of H_2O and extracted with EtOAc (3 × 50 mL). The combined organic layer was dried (Na_2SO_4), filtered and concentrated. The residue was purified using PTLC (Hex/EtOAc/HOAC 89:9:2, v/v) and eluted from the silica with MeOH/EtOAc (10:90, v/v), as described above, to yield an orange oil (17.9 mg, 38.2%). ^{1}H NMR (CD_3CN, 400 MHz) δ (ppm): 8.40 (dd, *J* = 8.7 Hz, *J* = 8.7 Hz, 1H, ArH), 7.58 – 7.39 (m, 7H, ArH), 7.31 (dd, *J* = 7.5 Hz, *J* = 1.4 Hz, 1H, ArH), 7.21 (dd, *J* = 8.8 Hz, *J* = 3.2 Hz, 1H, ArH), 5.31 (s, 2H, -CH2). ^{19}F

NMR (CD_3CN, 376 MHz) δ (ppm): -64.70 (dd, *J* = 7.9 Hz, *J* = 2.2 Hz,). HRMS (EI) calculated for $C_{16}H_{12}NOF$: 253.0903 amu, observed: 253.0907 amu (101).

Synthesis of 2-fluoroquinolin-8-ol (cold compound as a reference standard)

Compound 8-(benzyloxy)-2-fluoroquinoline (35.8 mg, 0.141 mmol) was dissolved in anhydrous CH_3CN (5 mL) and transferred into a 10 mL glass V- vial with Teflon septum and screw cap. Pd $(OH)_2$ (19mg) and Pd/C (19 mg) were added into the vial followed by pressurization with a balloon filled with H_2 (g). The reaction mixture was stirred for 1 h at room temperature. It was then filtered and washed through diatomaceous earth (Celite 545). The filtrate was concentrated under reduced pressure to yield a dark brown viscous solid (12.9 mg, 55.9%). ^{1}H NMR (CD_3CN, 400 MHz) δ (ppm): 8.44 (dd, *J* = 8.9 Hz, *J* = 7.9 Hz, 1H, ArH), 7.68 (bs, 1H, $\Delta\upsilon_{1/2}$ = 4.6 Hz, -OH), 7.50 -7.49 (m, 2H, ArH), 7.25– 7.21 (m, 2H, ArH). ^{19}F NMR (CD_3CN, 376 MHz) δ (ppm): -66.07 (d, *J* = 6.2 Hz). HRMS (ESI) calculated for C_9H_7FNO (+): 164.0512 amu, observed [M+H]: 164.0506 amu. This compound was used for *in vitro* fluorescence imaging studies (101).

Radiochemistry: preparation of reactive [^{18}F] Fluoride

Fluorine-18-labeled fluoride was produced by the ^{18}O (p,n) ^{18}F nuclear reaction, using a 17 MeV proton beam current to irradiate [^{18}O]H_2O (Cardinal Health), which was subsequently removed from the target and trapped on an anion exchange resin. The resin was eluted by back flushing with 1 mL of solution that contained potassium carbonate (9.8 mM) and 1:9 H_2O/MeOH (v/v) into an open glass test tube with 15 mg of 2,2,2-crypt (Kryptofix®) as previously described (102). The test tube was placed in a 100 ^{o}C oil bath and the mixture was azeotropically dried with anhydrous CH_3CN (1.5 mL) under nitrogen flow. 8-benzyloxy-2-chloroquinoline (3.0 mg, 0.011 mmol) dissolved in DMSO (0.25 mL) was transferred into the test tube with dry [K222][^{18}F].

The reaction mixture was briefly vortexed and placed in a 135 ^{o}C oil bath for 15 min. The test tube was removed from the heat and 5 mL of H_2O was added before being loaded onto a tC18 Sep-Pak (Waters pre-activated with 5 mL of CH_3CN and 5 mL of water). The Sep-Pak was rinsed with 5 mL of H_2O and eluted with anhydrous CH_3CN (1 mL) into a septum-sealed V-vial containing $Pd(OH)_2$ (8 mg) and Pd/C (8 mg). The reaction mixture was stirred at room temperature for 15 min under the pressure of a H_2 balloon. The reaction mixture was then diluted with 1 mL of warmed anhydrous CH_3CN (ca. 60 ^{o}C) and filtered through Celite. The filtrate was diluted with 3 mL of H2O before loaded onto the reverse phase semi-preparative HPLC (XTerra®

C18 semi preparative column [10 X 250 mm, 10 µm], CH_3CN: ammonium formate buffer [0.1M], 3:7; flow rate, 4 mL/min; retention time, 12-14 min). The product, [^{18}F] 2-fluoroquinolin-8-ol, was eluted at 13.5 min. The product [^{18}F] 2-fluoroquinolin-8-ol was isolated in 30 ± 4% (n=20) radiochemical yield (uncorrected for decay) in an overall time of 71 min, including formulation. The HPLC fraction containing [^{18}F] 2-fluoroquinolin-8-ol was diluted with 2 mL USP 8.4% sodium bicarbonate solution and 23 mL H_2O and loaded onto a t-C18 plus Sep-Pak® cartridge, (Waters; pre-activated with 10 mL EtOH followed by 10 mL H_2O). The C18 cartridge was then washed with 5 mL H2O and eluted with 1 mL EtOH, followed by 1 mL saline into a glass dose vial, fitted with a rubber septum and vent needle. HPLC analysis of formulated [^{18}F] 2-fluoroquinolin-8-ol revealed high radiochemical (>99%) and chemical purities of [^{18}F] 2-fluoroquinolin-8-ol. The specific activity of the formulated product was 1248 mCi/µmol, and the log D was 2.07 ± 0.03 for [^{18}F] 2-fluoroquinolin-8-ol, as measured using previously published method (103).

2.3. Results and discussion

The radio-synthesis of [^{18}F] 2-fluoroquinolin-8-ol was completed in 71 min (Fig. 1), with an uncorrected radiochemical yield of 30 ± 4% (n = 20). The isolated product was obtained in high specific activity (1.3 Ci/µmol) and high radiochemical purity (>99%) at the end of synthesis. Lipophilicity is

often a predictor of the ability of a compound to cross the blood-brain barrier, and is therefore an important factor in determining the feasibility of new radiopharmaceuticals that target the central nervous system (101). The measured log *D* (104) of [18F] 2-fluoroquinolin-8-ol was determined to be 2.07 ± 0.03, and is considered to be in the ideal range for brain penetrating compounds (105).

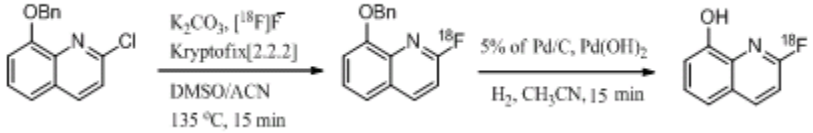

Fig. 1. Synthesis and radiolabeling of 2-F-8-HQ.

3. *In vitro* evaluation of 2-F-8-HQ

3.1. Background

High concentrations of zinc (up to 1 mM) have been found within amyloid plaques (56), which are thought to have been released from glutamatergic synapses (106). They reported the concentration (ug/g), of Zn 86.8±21.0, iron 53.1±13.7 and copper 30.1± 11.0, in senile plaque cores compared to control neuropil (Zn 22.6±2.8, iron 18.9±5.3 and copper 4.4±1.5) as measured by micro PIXE (particle induced X-ray emission) analysis. Watt et al. have reviewed the role of zinc in Alzheimer's disease (107). They report the crucial role for zinc in Aβ aggregation which is the most well-established contribution that zinc may have involved in AD pathogenesis, whilst, copper and iron appear to be primarily responsible for the toxicity of Aβ via oxidative stress-type mechanism (108, 109). Hydroxy quinolines are known to bind to di and trivalent metals (110, 111, 112) and can form a ternary complex with Aβ-zinc (92). Based on these reports we focused our studies on binding of 2-F-8-HQ to zinc and Aβ-zinc aggregates.

Hydroxy quinoline derivatives have been used in extensive applications as analytical reagents, because of their capability to form metal complexes with many metals producing a measurable fluorescent light. Their excitation and emission fluorescence spectra with and without metals, and the effect of solvents on their fluorescence intensity were characterized (113, 114,

115). For example, the ability of detecting zinc in brain sections with such compounds, the selectivity to detect magnesium in living cells and histochemical staining for calcium were all demonstrated (115, 116). Upon chelating zinc and other metals, they exhibit intense fluorescent emission (117).

Using conventional spectrofluorometer, 2-F-8-HQ was found to have an absorption maximum at 291 nm and it did not change with addition of equimolar amounts of zinc or Fe^{2+}. However, the absorption peak changed to 363 nm on addition of Cu^{2+} indicating binding of the ligand to Cu^{2+} (Fig. 2) . 2-F-8-HQ has fluorescence emission at 420 nm and fluorescence intensity did not change with addition of equimolar amount of zinc ions (Fig. 3). Zn forms fluorescent complex with 2-methyl-8-hydroxy quinoline (MeHQ) with absorption at 400 nm and emission at 530 nm (Fig. 4). MeHQ and TSQ N-(-6-methoxy-8-quinolyl)-para-tolunesulfonamide) had been used for assaying histochemically reactive zinc in the mice brain by Frederickson et al. (115).

Fluorescence emission of MeHQ is enhanced on combining with zinc whereas 2-F-8-HQ does not produce the similar effect, may be due to the presence of highly electronegative fluorine atom in the molecule. Since we could not use the conventional spectrofluorometer for fluorescence assays, and with limited availability of the compound, we evaluated Zn binding properties of the compound with an alternative approach. In this approach we

utilized a home built high sensitivity, electron multiplying CCD (charge coupled device) camera to measure the total light intensity emitted from a small (10 micro liter) sample using fluorescence imaging technique.

3.2. Hypothesis

2-F-8-HQ can bind to metals and form a metal complex. In addition, it can bind to the plaque aggregates through interaction with zinc.

3.3. Materials and methodology

3.3.1. Fluorescence metal binding studies

2-F-8-HQ was prepared by dissolving in ethanol (12mM) and diluting with HEPES buffer (50mM) to reach a final concentration of 100µM (PH=7.4). Then, equimolar amount of $ZnCl_2$ which dissolved in MQ water (0.1M) was added to the compound. The maximum UV absorption spectra of 2-F-8-HQ-Zn was measured by a Spectrophotometer (Shimadzu® UV-2401PC UV-VIS) and was found to be optimum at 290 nm.

For the fluorescence studies, high sensitivity electron-multiplying CCD camera (Princeton Instruments/ACTON PhotonMAX 512B with the e2v CCD97 sensor, 512×512 pixels) connected to a computer, mounted in a vertical orientation on an x-y-z stage with a lens of 25.4-mm (Schneider Xenon) was used to record the fluorescent light (118). Fiber coupled LED at 290 nm was used to excite the sample (LLS-290, 290 nm, FWHM 12 nm) with a maximum drive current CW at 30mA and 20 µW power. Aliquot

(10µl) of samples was used and placed over a quartz slide (76.2mm x 25.4mm, 1mm thick). The sample then was exposed for 1 min and the data were collected at a rate of 5 MHz. This was obtained by illuminating the sample from the top (the beam was angulated so the maximum light intensity would reach the sample) and the detected light intensity was recorded and subtracted from the background (slide without sample). All experiments were done in a light-tight box (Fig. 5).

To test the fluorescence intensity in different solvents, 2-F-8-HQ was prepared by dissolving in ethanol (12mM) and $ZnCl_2$ was dissolved in MQ water (0.1M). The metal complex was tested in different buffers including HEPES, TRIS, PBS with a concentration of 50mM. First, the fluorescence intensity of 2-F-8-HQ alone was examined. Second, equimolar ratio (1:1) of 2-F-8-HQ and $ZnCl_2$ was prepared. Then, 25µl of the metal complex (2-F-8-HQ –Zn) was added to 25µl of the buffers. Finally, 10µl aliquot was placed over the quartz slide and tested. In addition, buffers alone were tested to check for the changes in the detected light intensity.

It is well established that the metal complex with quinoline derivatives is more stable with a stoichiometric ratio of 2:1 (119). To examine the saturation of the fluorescence intensity of the metal complex, 2-F-8-HQ was prepared by dissolving in ethanol (12mM) and different concentrations were made by dilution with HEPS (50mM). $ZnCl_2$ was dissolved in MQ water (0.1M) and

diluted with HEPES to reach a final concentration of 3mM. Constant amount of $ZnCl_2$ was titrated with different concentrations of the ligand 2-F-8-HQ. The experiment was done in triplicate and data were fitted into binding-saturation equation using GraphPad Prism® software.

$$Y = Bmax \times X^h/(K_d^h + X^h)$$

Bmax: maximum binding, h: Hill slope, Kd: dissociation constant

In addition, EDTA which is non fluorescent (120) strong chelator with a high affinity to Zn in comparison to other metals (121) was used to quench the fluorescence intensity of 2-F-8-HQ –Zn and to demonstrate the inhibition of forming the metal complex (2-F-8-HQ –Zn). EDTA (4.5mg) was prepared by dissolving in MQ water with the addition of NaOH to reach a final volume of 1ml with 12mM concentration. EDTA, 2-F-8-HQ and $ZnCl_2$ were diluted with HEPES to reach a final concentration of 5mM. 2-F-8-HQ –Zn was formed (2:1) and EDTA was added to the complex as half the amount of 2-F-8-HQ (20µl of 2-F-8-HQ: 10µl of $ZnCl_2$: 10µl of EDTA) to reach a final volume of 40µl.

3.3.2. Aβ-Zn aggregates binding studies

Aβ peptide-Zn aggregates were prepared by incubating $ZnCl_2$ (25 µM) in buffer PBS (pH 7.4) with Aβ peptide 1–42 (25 µM) (Bachem Inc.) while stirring at room temperature for 1 hour. To ensure the aggregation of Aβ peptide, the mixture was incubated at 37 °C for 48 h (92).

The radiolabeled 2-F-8-HQ of different concentrations (10 and 5 uL of 417nM, 41.7nM and 4.17nM respectively) was added to 10 uL of Aβ-Zn (100uM) and PBS to reach a final volume of 1 mL. The experiment was done in triplicate, and the different concentrations of the radiolabeled-compound were incubated with Aβ-Zn for 30 min. The same procedure was repeated without adding Aβ-Zn to determine the non specific binding. All tubes were centrifuged for 10 minutes and the supernatant removed. The aggregates were washed again by adding 1 mL of PBS and centrifuging. Radioactivity in the aggregates was measured by a well type gamma counter (Perkin Elmer). Then data were fitted into binding-saturation equation using GraphPad Prism® software.

$$Y = Bmax \times X^h/(K_d^h + X^h)$$

Bmax: maximum binding, h: Hill slope, Kd: dissociation constant

3.3.3. Brain sections autoradiography imaging

Frozen brains sections of AD (12 months) and age matched control mice were cut in a cryostat at 10 µm thicknesses. Brain sections were incubated with 200µL of 2-F-8-HQ (50µCi/ml) for 30 min. The slides were washed with PBS and air dried. Then, they were exposed to Phosphor imaging plate for 2 hrs in the dark and images were quantified (PerkinElmer Cyclone® Storage Phosphor Imaging System). Image intensities were expressed as digital light unit (DLU/mm^2) corrected for the background.

3.3.4. Immunohistochemistry

Following the autoradiography experiment, the same brain sections were stained with rabbit polyclonal anti-serum against Aβ-42 followed by Alexa488 labeled second antibody as described previously (122). Briefly, the brain sections were dried and fixed for 4h in paraformaldehyde and washed in PBS after incubation with Aβ-42 antibody and then with Alexa488 labeled second antibody. Finally, the sections were washed in PBS and viewed under a fluorescence microscope. Plaque density was quantified as previously described using Image J (NIH) software (122). Briefly, plaque regions were specified and both area (pixels) and signal intensities were obtained. The plaque density was defined as the plaque area multiplied by the average plaque intensity.

3.4. Results and discussion

Fluorescence studies of metal complexes

Fluorescence imaging showed different solvents (buffers) had significant influence on the fluorescence intensity of the metal complex (Fig. 6). The results showed no significant changes for solvents alone or by themselves and they were similar to the quartz slide alone (Q slide). The signal intensity of 2-F-8-HQ seems to increase upon binding to zinc. In addition, HEPES buffer has shown to improve the signal intensity in comparison to the other solvents (Fig. 6). There was a significant difference

between the measurements ($P<0.0001$). The binding affinity saturation curve ($R^2=0.94$) showed the maximum fluorescence intensity at (2:1) ratio (Fig. 7). Upon adding EDTA to 2-F-8-HQ –Zn, the fluorescence intensity was reduced to a level similar to the 2-F-8-HQ alone (Fig. 8), which demonstrates the competition in binding to zinc ($P<0.0001$).

The binding study results strongly suggest the affinity of 2-F-8-HQ to the Zn. The increased fluorescence intensity at 2:1 ratio is concurrent with previous results regarding the stability of the metal complexes with a stoichiometric ratio of 2:1 (119). Addition of EDTA as a strong chelating agent demonstrated the inhibition of the 2-F-8-HQ –Zn formation, which was indicated as a marked reduction in the fluorescence intensity to a level similar to the fluorescence intensity of 2-F-8-HQ alone.

Solvents effect on the variation of the fluorescence intensity of hydroxy quinoline derivatives upon binding to metals has been reported (123, 124, 125). In our study, we found HEPES to be the optimal among other buffers in terms of producing the highest fluorescence intensity. Although we were able to demonstrate the binding affinity to zinc in mM range, the system sensitivity was limited in detecting the binding affinity in lower concentrations due to the low power of the exciting source (20 μW). In addition, the presence of the fluorine atom may have reduced the fluorescence intensity of the compound. We found that the optimal excitation and emission for 2-F-8-HQ about 290mn

and 420nm respectively, while it was reported as 395nm and 540nm respectively for 8HQ (115).

Binding affinity to Aβ-Zn aggregates

The results showed high affinity to Aβ -Zn with a Kd value of 1.5nM. The curve fitting showed that the Hill slope value is 2.2, which indicates that the receptor or the ligand has multiple binding sites with positive cooperativity (Fig. 9). The Kd value (table. 1) is within the range reported (0.5-3.7nM) for previous amyloid plaques targeting agents (92, 126).

Autoradiography

Autoradiography images (Fig. 10) showed higher uptake for AD brain sections in comparison to control (P=0.002). In addition, regional analysis for autoradiography (Fig. 11) demonstrated higher activity for the cortex and the cerebellum of AD mice brain sections in comparison to control mice brain sections (P=0.0018).

Immunohistochemistry

The results showed variation in the plaques density (P=0.0149**)** in different regions of AD brain sections including cerebral cortex, hippocampus and the cerebellum (Fig. 12) while control mice showed negative results (absence of any plaques).

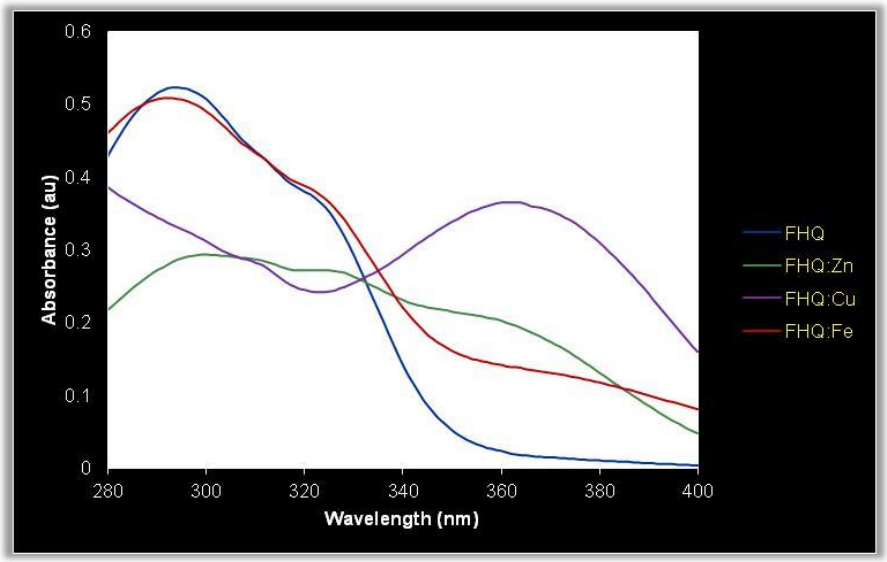

Fig. 2. Absorption spectra of 2-F-8-HQ with different metals.

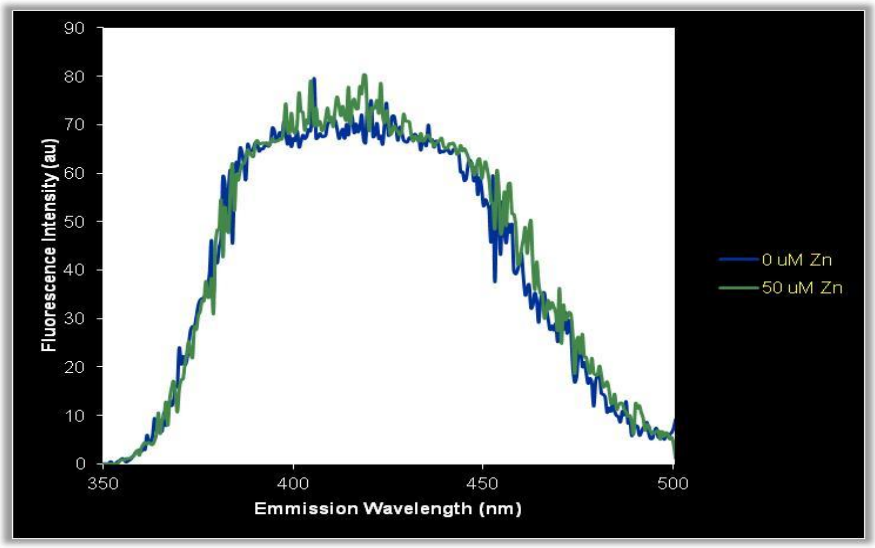

Fig. 3. Emission spectra of 2-F-8-HQ with addition of Zn.

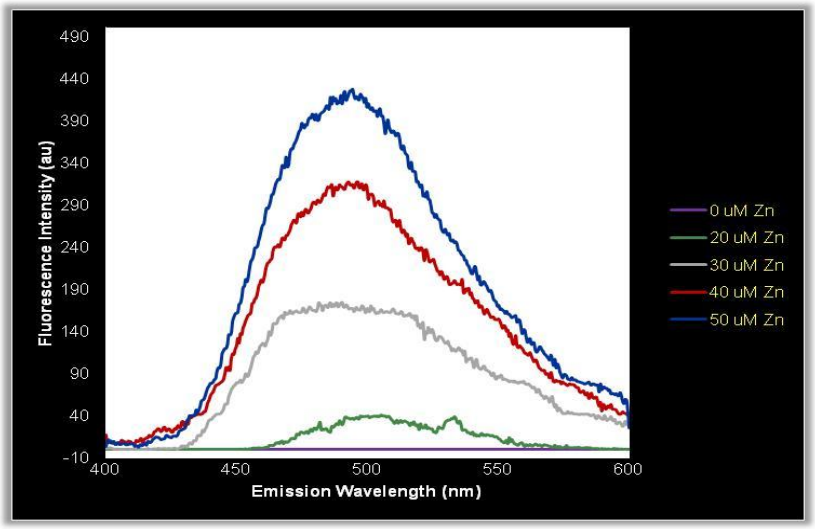

Fig. 4. Emission spectra of MHQ with addition of Zn.

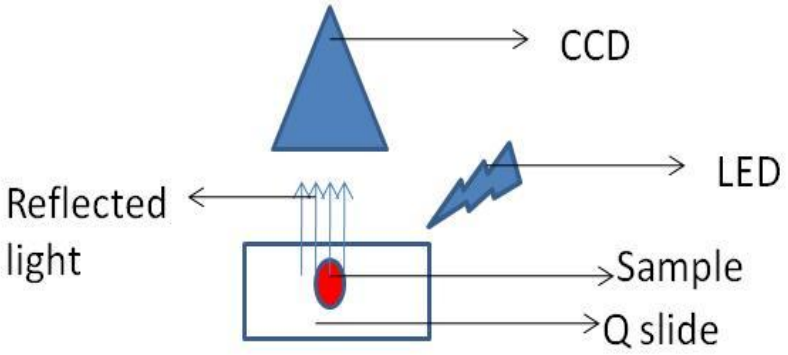

Fig. 5. A schematic diagram represents the set up for the fluorescence imaging experiment.

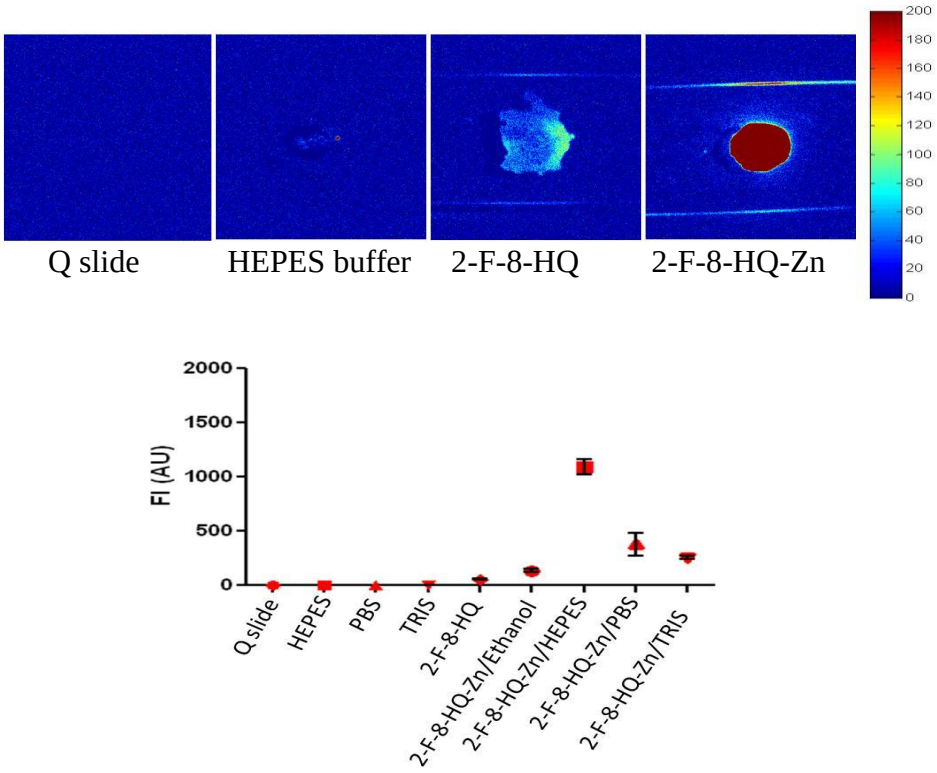

Fig. 6. Fluorescence intensity [FI (AU)] (arbitrary unit), of 2-F-8-HQ, Zn-quinoline complex in different buffers and buffers alone. The values represent the mean (n=10) signal intensity (±SE).

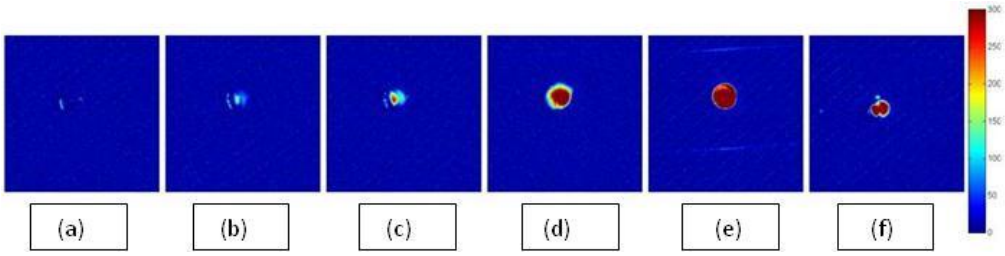

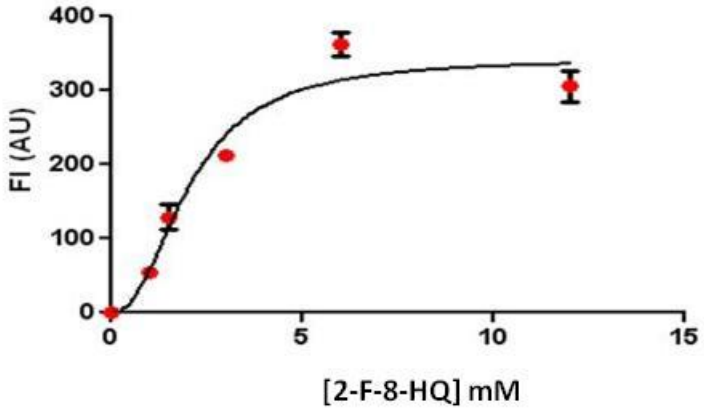

Fig. 7. The images (a-f) arranged from left to right (0mM, 1mM, 1.5mM, 3mM, 6mM and 12mM) as the concentration of 2-F-8-HQ increases with a constant concentration of Zn^{2+} (3mM). The maximum light intensity occurred at 2:1 ratio. Data represent mean (n=3) fluorescence intensity ±SE.

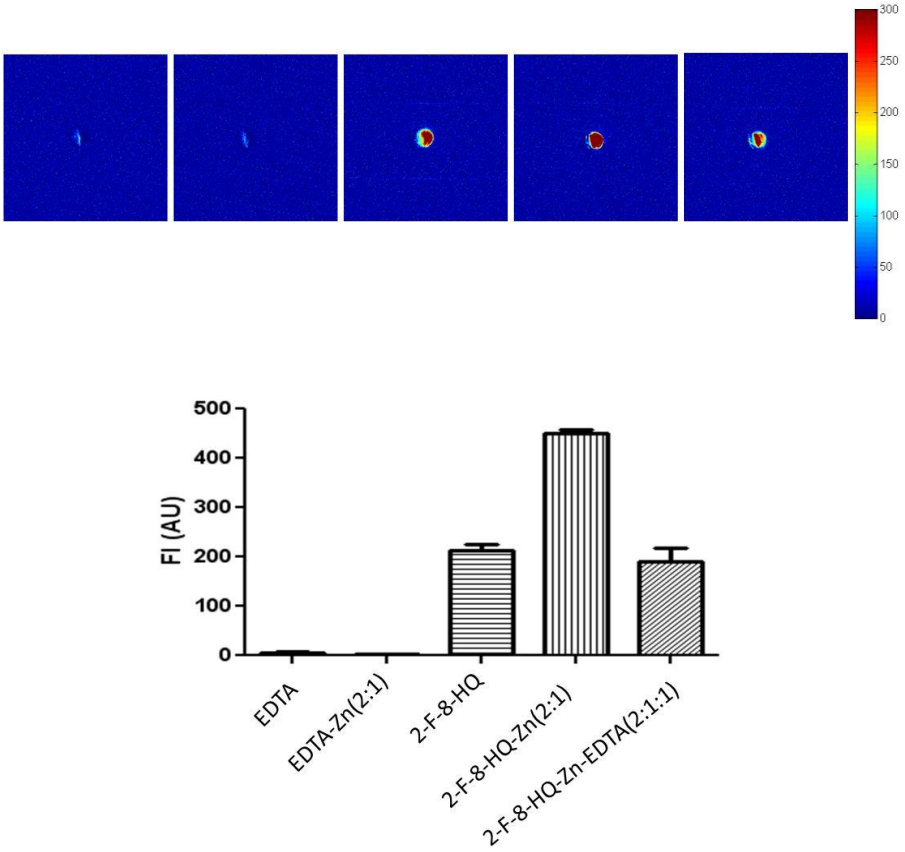

Fig. 8. Fluorescence intensities correspond to EDTA, EDTA-Zn 2:1, 2-F-8-HQ, 2-F-8-HQ-Zn 2:1, and 2-F-8-HQ: Zn: EDTA 2:1:1, respectively. The graph shows the changes of the FI upon adding EDTA to 2-F-8-HQ-Zn and compares the FI of the chelators and the metal complexes. Data represents the mean FI ±SE (n=3).

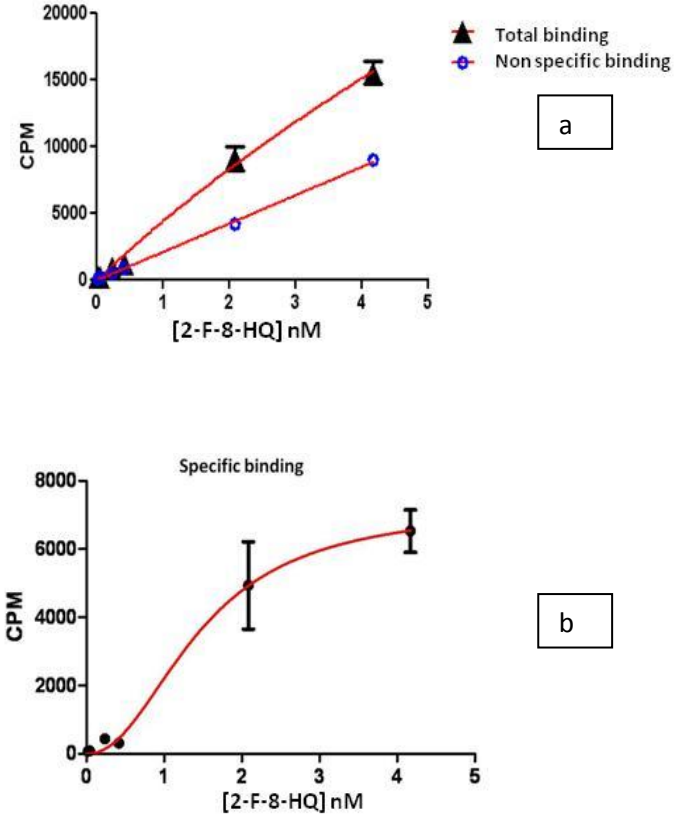

Fig. 9. *In vitro* binding study. The first graph (a) shows the total and the non specific binding. The second graph (b) shows the specific binding after subtraction (total-nonspecific binding) and curve fitting. Data represent mean CPM (n=3) ± SE.

Bmax	7229 CPM
h	2.15
Kd	1.466 nM
95% Confidence Intervals	
Bmax	4640 to 9818
h	0.3016 to 3.999
Kd	0.6150 to 2.316
Goodness of Fit	
R square	0.908

Table. 1. Summarizes the statistics and the parameters values of the curve fitting of the specific *in vitro* binding study.

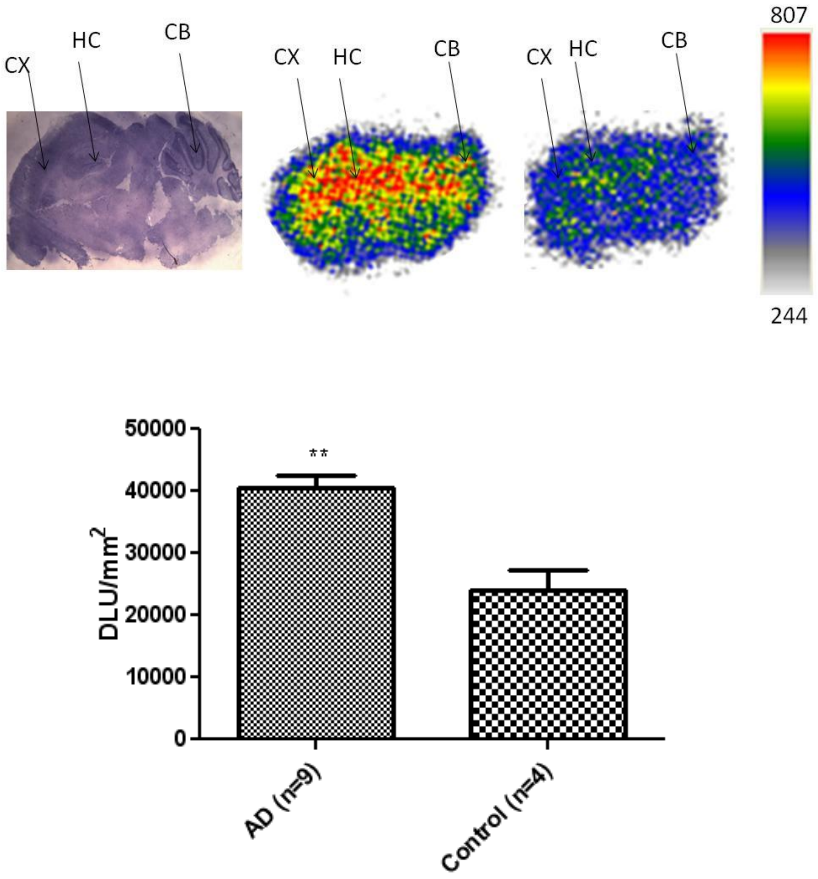

Fig. 10. *In vitro* autoradiography. Brain cross section images is correlated with AD and control mice brain showing higher activity in the AD brain in comparison to control in the labeled regions. Quantification of the activity in the total brain section showing significant difference between AD (n=9) and control (n=4) mice**.**

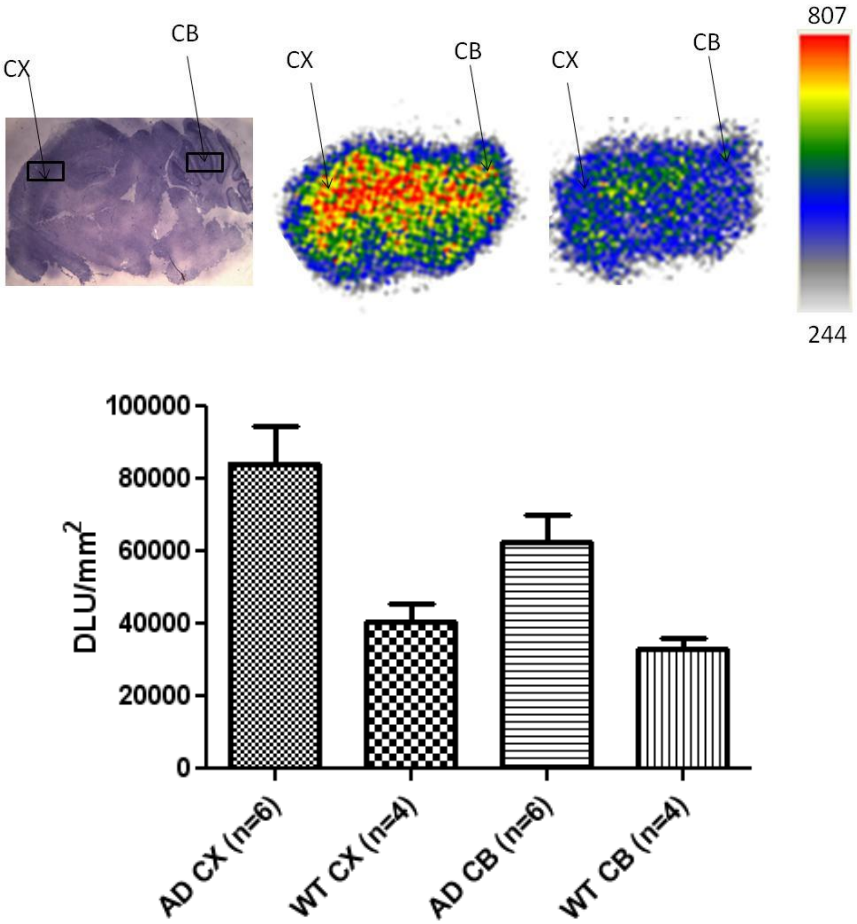

Fig. 11. *In vitro* autoradiography. Brain cross section images is correlated with AD and control mice brain showing higher activity in the cortex and the cerebellum AD brain regions in comparison to control as labeled. Quantification of the activity (CPM) in these regions showing significant difference between AD (n=6) and control (n=4) mice**.**

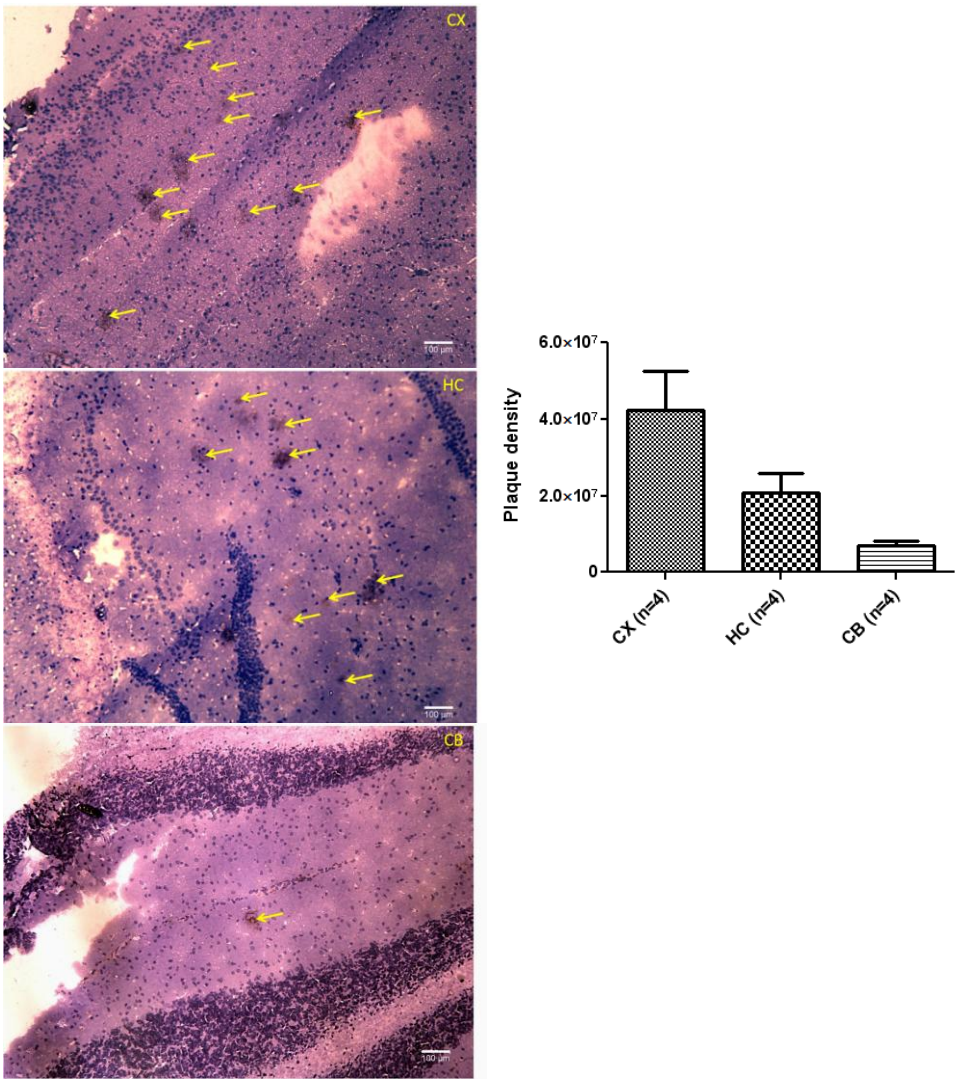

Fig. 12. Variation in the plaque density in different regions of the AD brain as labeled, and quantification of plaque density shows higher density in the cerebral cortex and the hippocampus than the cerebellum (n=4) ± SE.

4. *In vivo* PET imaging of 2-F-8-HQ

4.1. Background

Our previous studies showed that the uptake of I-125 CQ (clioquinol) in mice brains was low (~ 1 %). However, the uptake could be enhanced by encapsulating the tracer in burtylcyanoacrylate nanoparticles (100). Opazo et al. evaluated I-125 labeled clioquinol in control and AD transgenic (Tg2576) mice and I-123 labeled CQ in humans (92). Their data showed slight elevation of the tracer brain uptake in AD mice (compared to control mice) at 15 min post i.v. injection of the tracer. However, it was <1% ID/g in both the cases. SPEC imaging studies in humans volunteers (healthy and mild AD) with I-123 CQ were not encouraging as the tracer signal was too low to permit imaging. Tracer counting was possible in the cerebral hemispheres although counts were not sufficiently high to achieve reliable data from other brain regions such as the cerebellum (92).

It was reported that ^{11}C-PIB and [^{18}F]FDDNP have the potential to bind plaques in vitro and in human studies. However, they both failed to differentiate between control and AD mice *in vivo* (Fig. 13) (89).

This encouraged us to investigate the feasibility of differentiating AD and control mice, and the ability of the agents to detect different plaques densities at different ages of AD mice.

In addition, conventional analysis of brain uptake using CT images doesn't provide enough contrast to differentiate different brain regions. Although MRI imaging is needed to obtain a high anatomical image of the brain to distinguish uptake in different regions, it is expensive and time consuming. Accordingly, we evaluated the use of free available software (AMIDE) (127) combined with a 3D MRI mouse brain atlas (Fig. 14) (128) to segment the brain into distinct regions and quantify the activity uptake in suspected plaques regions.

4.2. Hypothesis

2-F-8-HQ can differentiate AD from WT mice *in vivo* by PET/CT imaging. Cerebral regions including olfactory bulb, cerebral cortex and hippocampus will show higher uptake than the cerebellum. Older mice will have more retention of the compound in comparison to younger and control mice.

4.3. Materials and methodology

4.3.1. Animal studies

Double transgenic mice with double mutation (APP/PS1) for Alzheimer's disease were used (Strain: B6C3-Tg) (APP_{swe}, PSEN1dE9)85Dbo/J). This particular model correspond to a form of early onset of disease and expresses mutant human presenalin 1 (DeltaE9) and a chimeric mouse /human amyloid precursor protein (APP_{swe}). Tg mice were

bred by Dr. QU in the campus and characterized by genotyping. Details of characteristics of these mice have been reported by Qu et. al (122). Control mice were of the same strain without gene transfection. Animals of both sexes were used. The weight of the animals was 35-45 grams. Groups of mice of different ages (4-12 months) were imaged in a Siemens Inveon® preclinical PET/CT imaging system.

4.3.2. Small Animal PET/CT Imaging

Small animal PET/CT imaging studies were performed using a Siemens Inveon® Multimodality PET/CT system (Siemens Medical Solutions Inc., Knoxville, TN, USA). Ten minutes prior to imaging, the animals were anesthetized using 3% Isoflurane at room temperature until stable vital signs were established. Once the animal was sedated, the animal was placed onto the imaging bed under 2% Isoflurane anesthesia for the duration of the imaging. The micro CT imaging was acquired at 80kV and 500 µA with a focal spot of 58µm. The PET images were acquired directly following the acquisition of CT data. Radiotracer (50-90 µCi) was injected intravenously via the tail vein. Immediately following the injection, a 20-30 minute dynamic scan was performed. PET images were reconstructed using Fourier Rebinning and Ordered Subsets Expectation Maximization 3D algorithm with dynamic framing every 60 seconds. Reconstructed images were fused and analyzed using Inveon® Research Workplace (IRW) software.

4.3.3. PET/CT image analysis

Collected PET/CT images of double mutated mice (APP/PS1) and wild type mice of different ages (4, 6, and 12 months) were analyzed using AMIDE software and a 3D mouse brain atlas. PET images (voxel volume: 0.9×0.9×0.8 mm) were overlaid on the CT images (voxel volume: 0.2×0.2×0.2 mm). The registration of the images was performed by identifying three anatomical regions (e.g. heart, kidneys and the brain) on both images. The brain region was segmented based on a 3D mouse brain atlas (voxel volume: 0.06×0.06×0.06 mm) into distinct areas where the plaques are mostly found.

These areas include olfactory bulb, cerebral cortex, hippocampus and to lesser extent cerebellum (129-133). 3D ROIs were selected to cover these regions in each plane including axial, coronal and sagittal plane (Fig. 15a-e). Then, standardized uptake value (SUV) of each region was calculated.

SUV = % ID/g tissue × Ws ÷ 100

Where ID is the injected dose, Ws is the subject weight (134). Time activity curves (TACs) were fitted into two phase exponential decay equation to calculate the decay parameters for both AD and control mice using MATLAB 7.9.0 (R2009b).

$a \times \exp(-b \times x) + c \times \exp(-d \times x)$

b, fast rate constant, fast half life (0.693/b)

d, slow rate constant, slow half life (0.693/d), a and c are coefficients

For statistical analysis, normalized SUV and area under curve (AUC) of the TACs were calculated for AD and control mice. Student's t-test was used to compare control group to AD group, and one way ANOVA to compare multiple groups using GraphPad Prism® software.

4.4. Results and discussion

Conventional PET/CT analysis

Analysis of PET images based on the CT image of the brain showed high uptake (%ID/g) in the AD (n=5: 10-12 months) and rapid clearance in the control mice (n=6: 10-12 months) for the total brain region with a significant difference at different time points (Fig. 16 and table 2). However, specific uptake in different brain regions was difficult to obtain due to the low CT image contrast.

PET/CT analysis using MRI brain atlas

Time activity curves (TACs) of AD mice (n=5:12-6 months old) showed more retention of the activity over 10 min in comparison to the control mice (n=3: 12 months old) for different regions of the brain including olfactory bulb, cerebral cortex, hippocampus and cerebellum (Fig. 17). Data were expressed as SUV normalized to the first time point. During the first 2 min, there was a rapid clearance of the compound. However, AD mice had slower clearance than the control mice (table. 3). The AUC of TACs for the

total brain showed significant difference (P= 0.0074) between AD and control mice (Fig. 20).

Age dependent brain uptake in AD mice

The retention for the total brain region of the older mice (12 months) was significantly higher (p=0.0147) than the younger mice (6 months) (Fig. 19). In addition, TACs of the 6-month AD mice demonstrated higher brain activity than the 4-month AD and the 4-month control mice (Fig. 18). There was a significant difference between the 6-month AD mice and the 4-month control mice (p=0.03). Longer retention time of the compound in the AD mice brains in comparison to controls was found (Fig. 21).

The regional analysis of the PET images demonstrated higher uptake in the regions associated with the plaques. In addition, cerebral regions have more activity than the cerebellum. Dynamic PET images demonstrated fast clearance of the compound in the normal brain and higher accumulation in the cerebral regions of the AD mice than the cerebellum region (Fig. 22). Integrated activity (0-600s) showed more retention of the compound in the older AD mice brains in comparison to younger and the control mice (Fig. 23a-b).

Hydroxy quinoline derivatives are weak chelating agents. They bind to transition metals such as zinc, copper and iron without resulting in metal depletion (135). Among biologically relevant metals in the brain, zinc was

found to be the most elevated metal in the AD brain mostly in the hippocampus and the cerebral cortex (49, 130).

However, the presence of zinc localized in the plaques of mice cerebellum was demonstrated (132). This supports the imaging results where the compound retention was higher in the cerebral regions in comparison to the cerebellum. In addition, normal brain showed some activity retention especially in hippocampus and the cortical regions. This finding could be related to the fact that most of the cheatable zinc is found in the cerebral regions and that very low amount of free zinc is available in the cerebellum of normal mice brain (136).

In addition a significant difference was noticed between 12- and 6-month old mice for the total brain uptake similar to what has been already reported about age-dependent plaques density as well as zinc levels (137, 106).

Regional analysis based on this method showed differences between control and AD mice at different ages. These results indicate a promising role of this compound for the early detection of AD and for differentiating different stages of the disease progression.

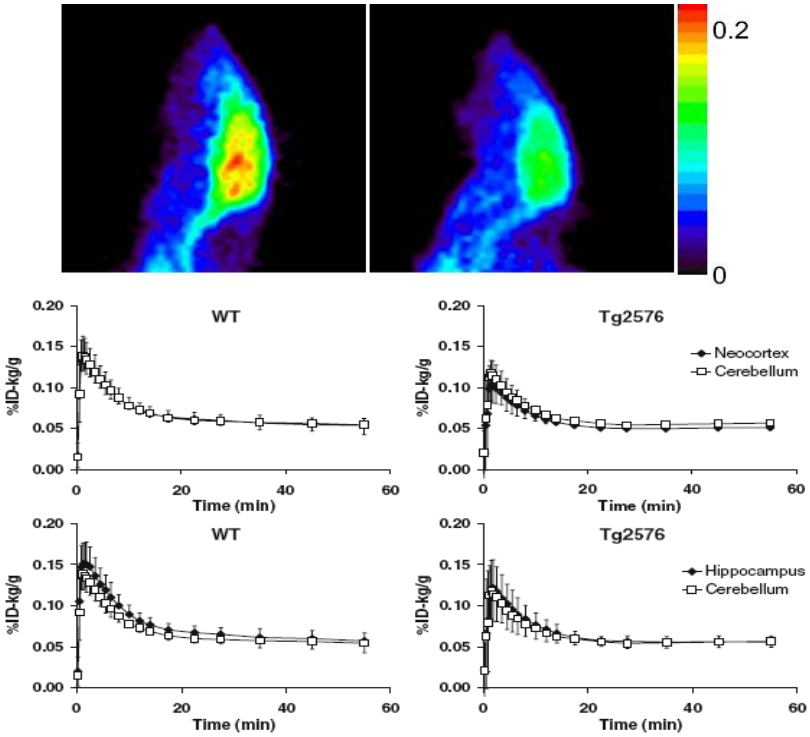

Fig. 13. [^{18}F]FDDNP shows no difference between AD (Tg2576,13-15months) and WT mice and no detected changes between cerebral regions and the cerebellum in terms of activity retention.
Kuntner, C. *et al.* Limitations of Small Animal PET Imaging with [^{18}F]FDDNP and FDG for Quantitative Studies in a Transgenic Mouse Model of Alzheimer's Disease. *Molecular Imaging and Biology* **11**, 236-240, doi:10.1007/s11307-009-0198-z (2009).

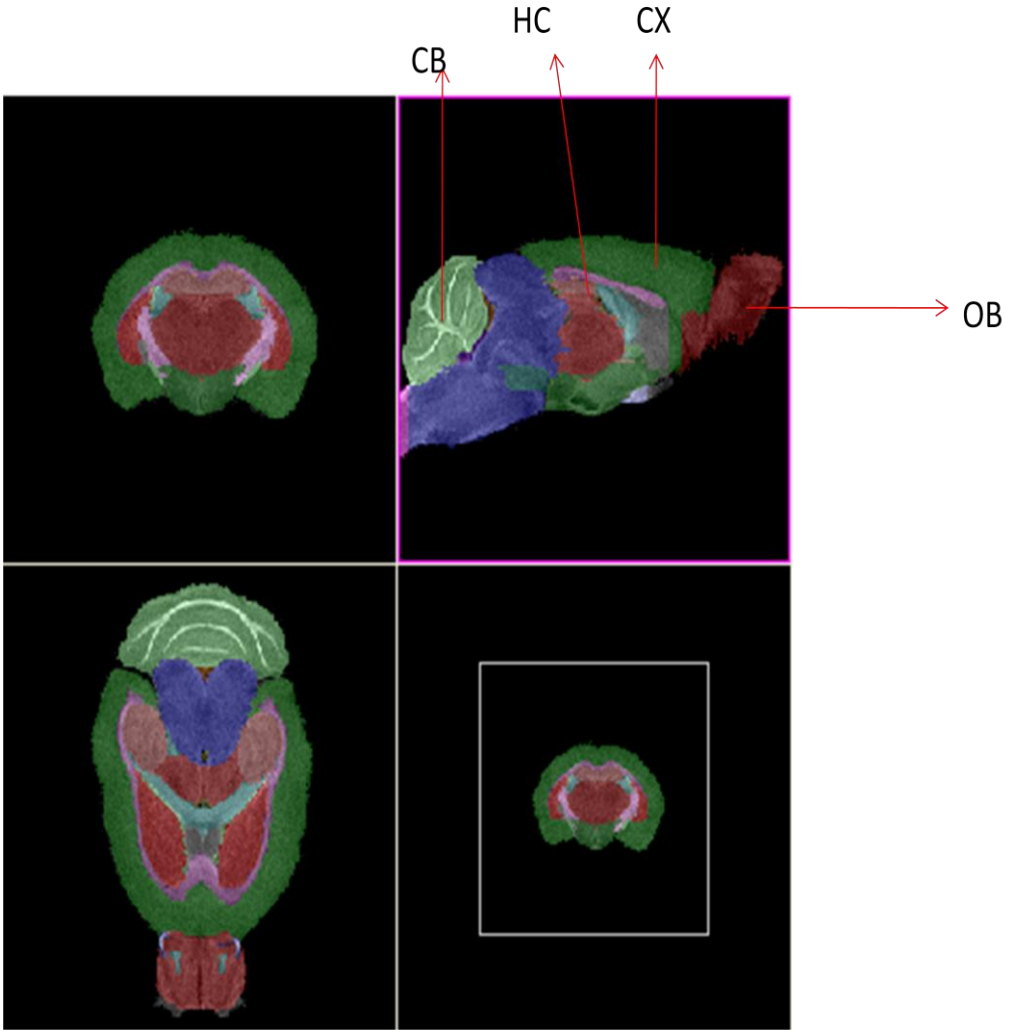

Fig. 14. MRI 3D mouse brain atlas; CB: cerebellum, HC: hippocampus, CX: cerebral cortex and OB: olfactory bulb. This atlas was generated using magnetic resonance microscopy (MRM), classical histology and immunohistochemistry.

MacKenzie-Graham, A. *et al.* The informatics of a C57BL/6J mouse brain atlas. *Neuroinformatics* **1**, 397-410, doi:10.1385/ni:1:4:397 (2003).

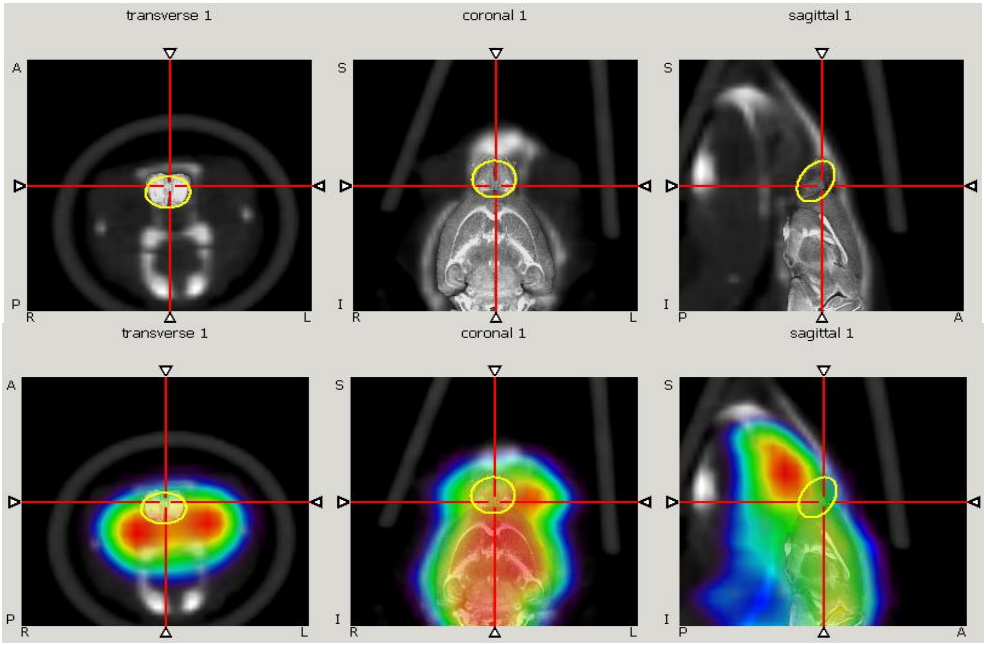

Fig. 15a. The first and the second rows are composed of 3 images; transverse, coronal and sagittal respectively. The first row shows the registration of CT and the brain atlas images. The second row shows the registration of PET/CT with the brain atlas. The 3D ROI shows the localization of the olfactory bulb region.

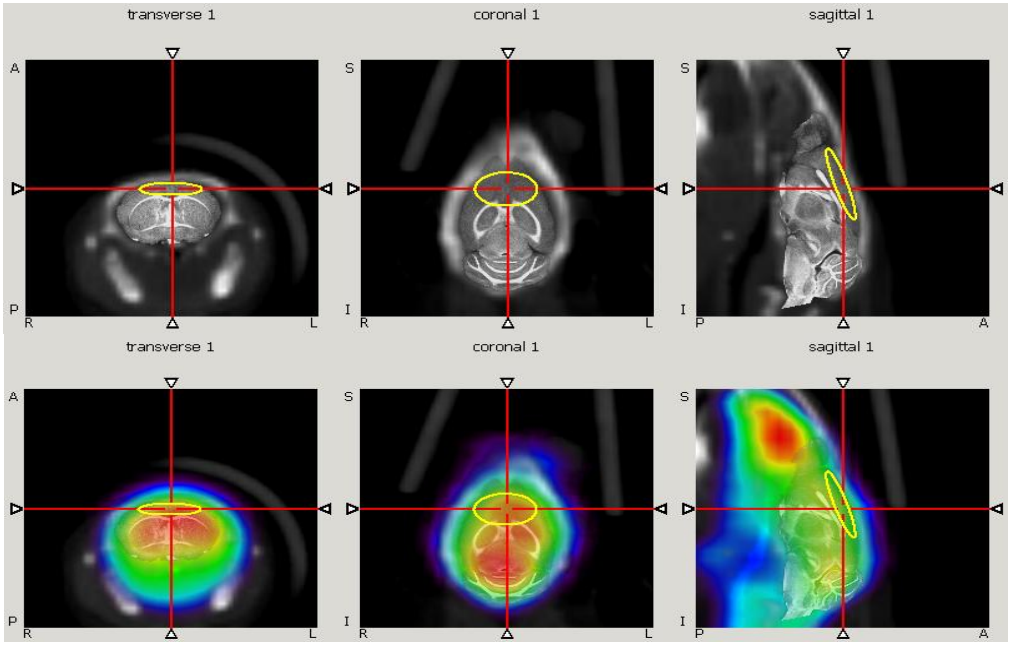

Fig. 15b. The first and the second rows are composed of 3 images; transverse, coronal and sagittal respectively. The first row shows the registration of CT and the brain atlas images. The second row shows the registration of PET/CT with the brain atlas. The 3D ROI shows the localization of the cerebral cortex region.

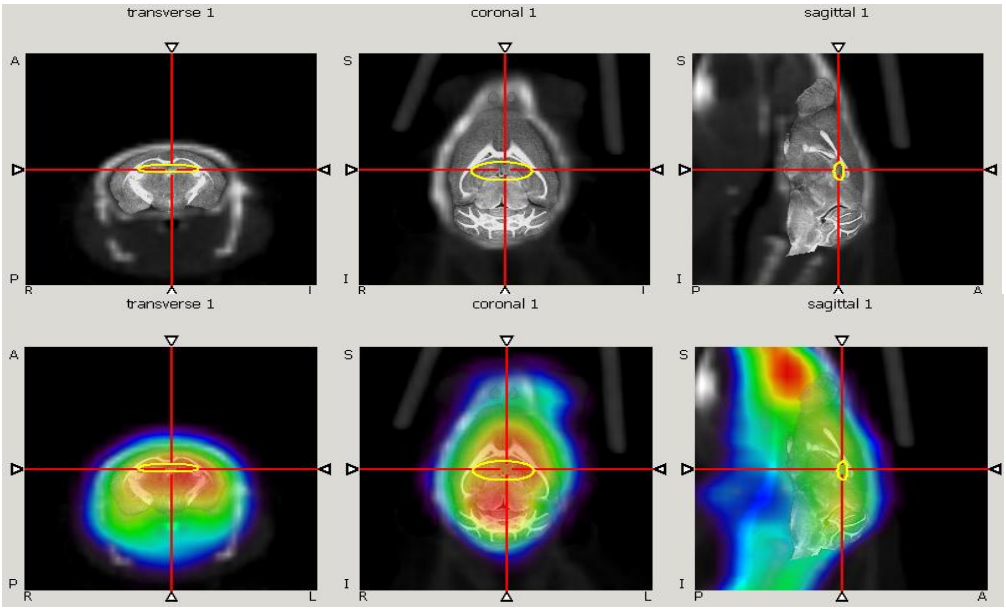

Fig. 15c. The first and the second rows are composed of 3 images; transverse, coronal and sagittal respectively. The first row shows the registration of CT and the brain atlas images. The second row shows the registration of PET/CT with the brain atlas. The 3D ROI shows the localization of the hippocampus region.

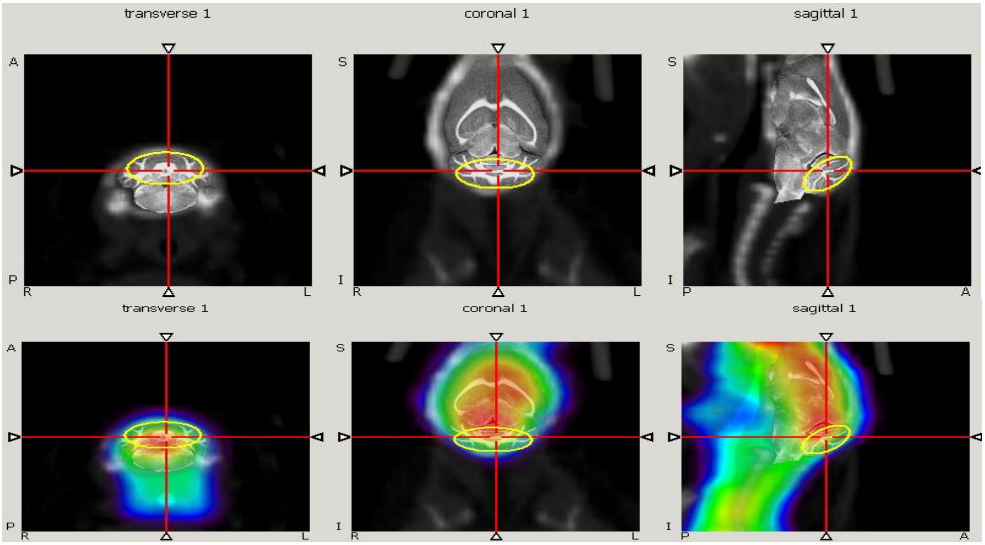

Fig. 15d. The first and the second rows are composed of 3 images; transverse, coronal and sagittal respectively. The first row shows the registration of CT and the brain atlas images. The second row shows the registration of PET/CT with the brain atlas. The 3D ROI shows the localization of the cerebellum region.

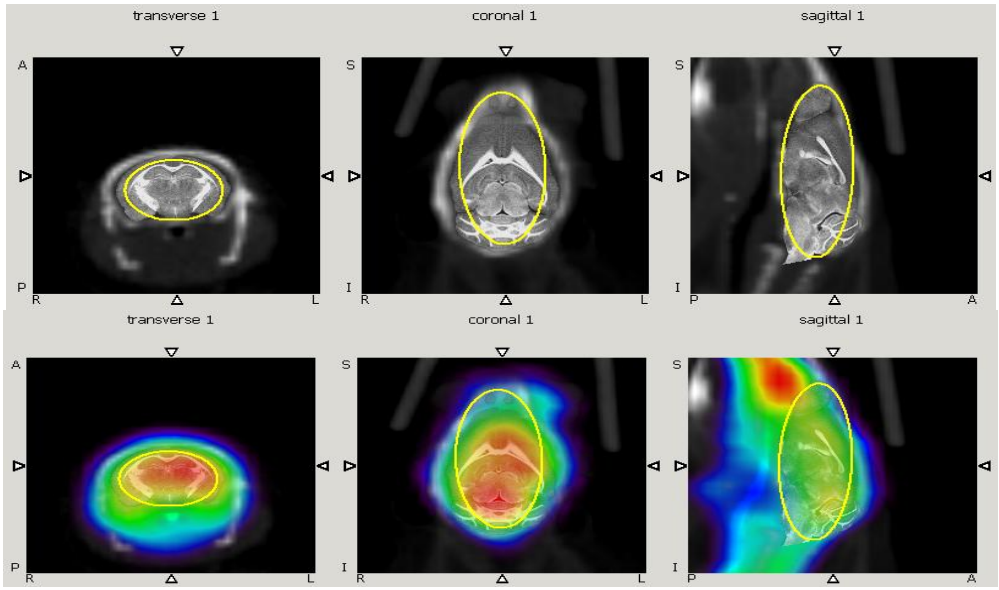

Fig. 15e. The first and the second rows are composed of 3 images; transverse, coronal and sagittal respectively. The first row shows the registration of CT and the brain atlas images. The second row shows the registration of PET/CT with the brain atlas. The 3D ROI shows the localization of the total brain region.

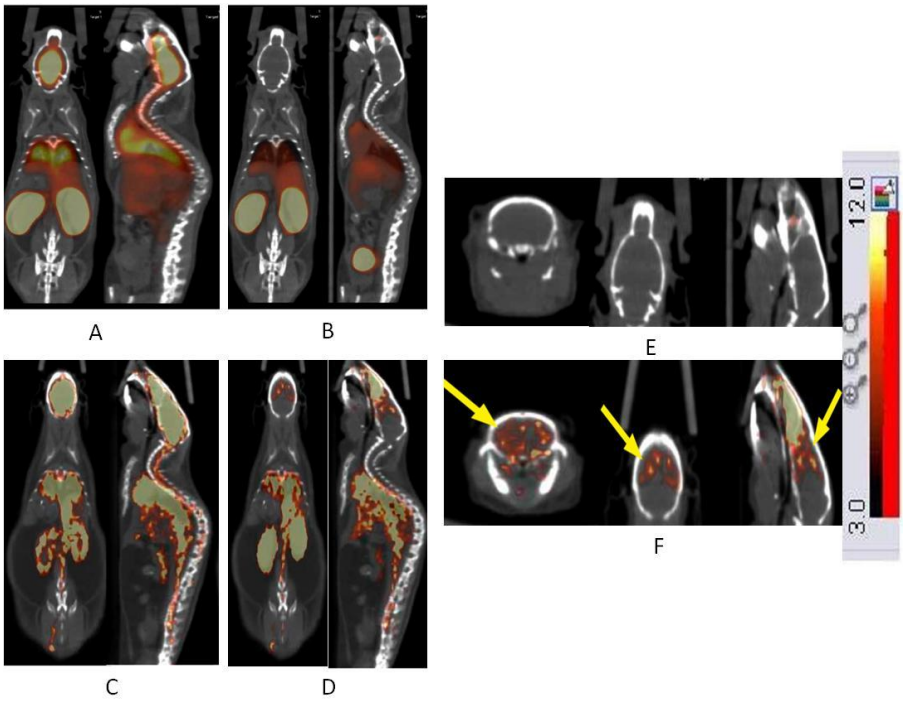

Fig. 16. Control mice images at 0.5-1.5min post injection (A) and at 3.5-4.5min post injection. AD mice images at 0.5-1.5min post injection (C) and at 3.5-4.5min post injection (D). Control mice brain section in different views (E) in comparison to the AD mice (F). Units of the scale bar represent the %ID/g.

%ID/g					
Time (min)	5	10	15	20	30
AD (n=5)	4.81±1.45	4.08±1.42	3.58±1.36	3.23±1.07	2.71±0.91
WT (n=6)	2.10±0.86	1.66±0.76	1.44±0.70	1.24±0.66	1.06±0.61
P<0.05	0.012	0.011	0.009	0.007	0.005

Table. 2. Summarizes the %ID/g of AD and control mice in whole brain and the statistical analysis at different time points.

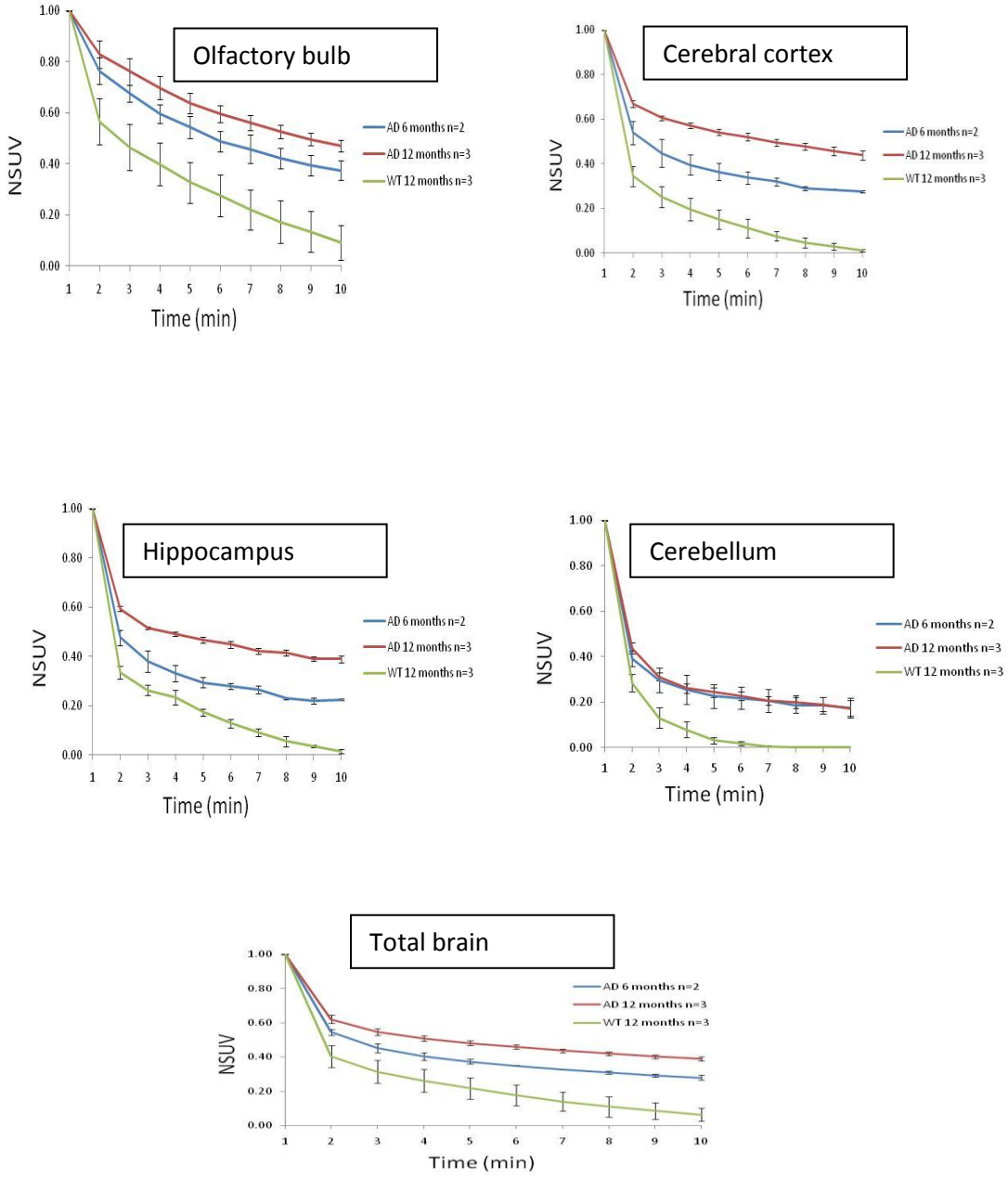

Fig. 17. Data represent mean SUV normalized to the first time point ± the SE in each region of the brain for AD and control mice as labeled in each graph.

Mouse age and type	**2 min**	**5 min**	**10 min**
12 months (n=3), AD	0.62 ±0.03	0.48±0.01	0.39±0.01
6 months (n=2), AD	0.55±0.02	0.37±0.01	0.28±0.01
12 months (n=3), WT	0.4±0.06	0.22±0.06	0.06±0.04

Table. 3. Total brain uptake (mean normalized SUV± SE) at different time points.

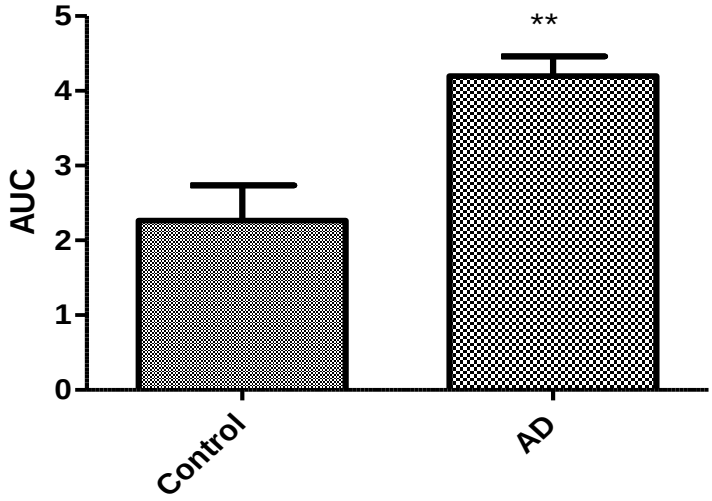

Fig. 18. Student's t-test shows significant difference between control (n=3) and AD mice (n=5) (P= 0.0074). Data represent the mean AUC of TACs ± SE over 10 min.

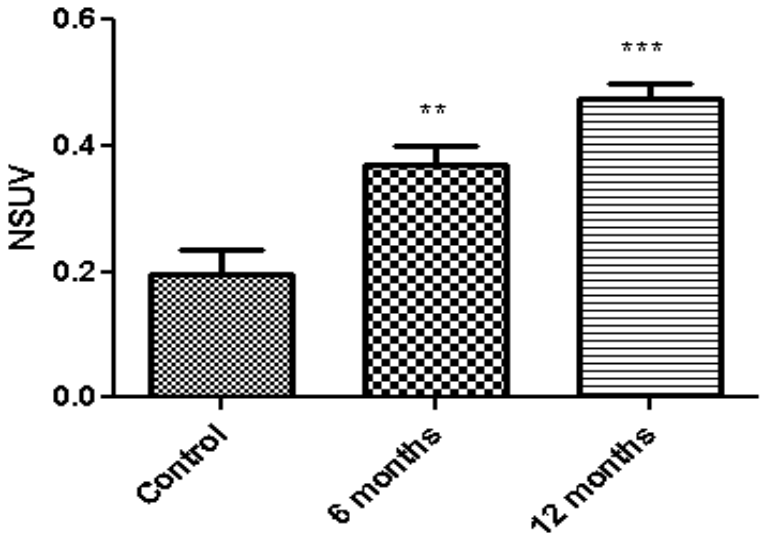

Fig. 19. Student's t-test shows significant difference between groups; control Vs 12 months AD ($P < 0.0001$), control Vs 6 months AD ($P=0.0020$) and 12 months Vs 6 months ($P=0.0147$) respectively. Data represent the mean normalized SUV of TACs ± SE over 10 min.

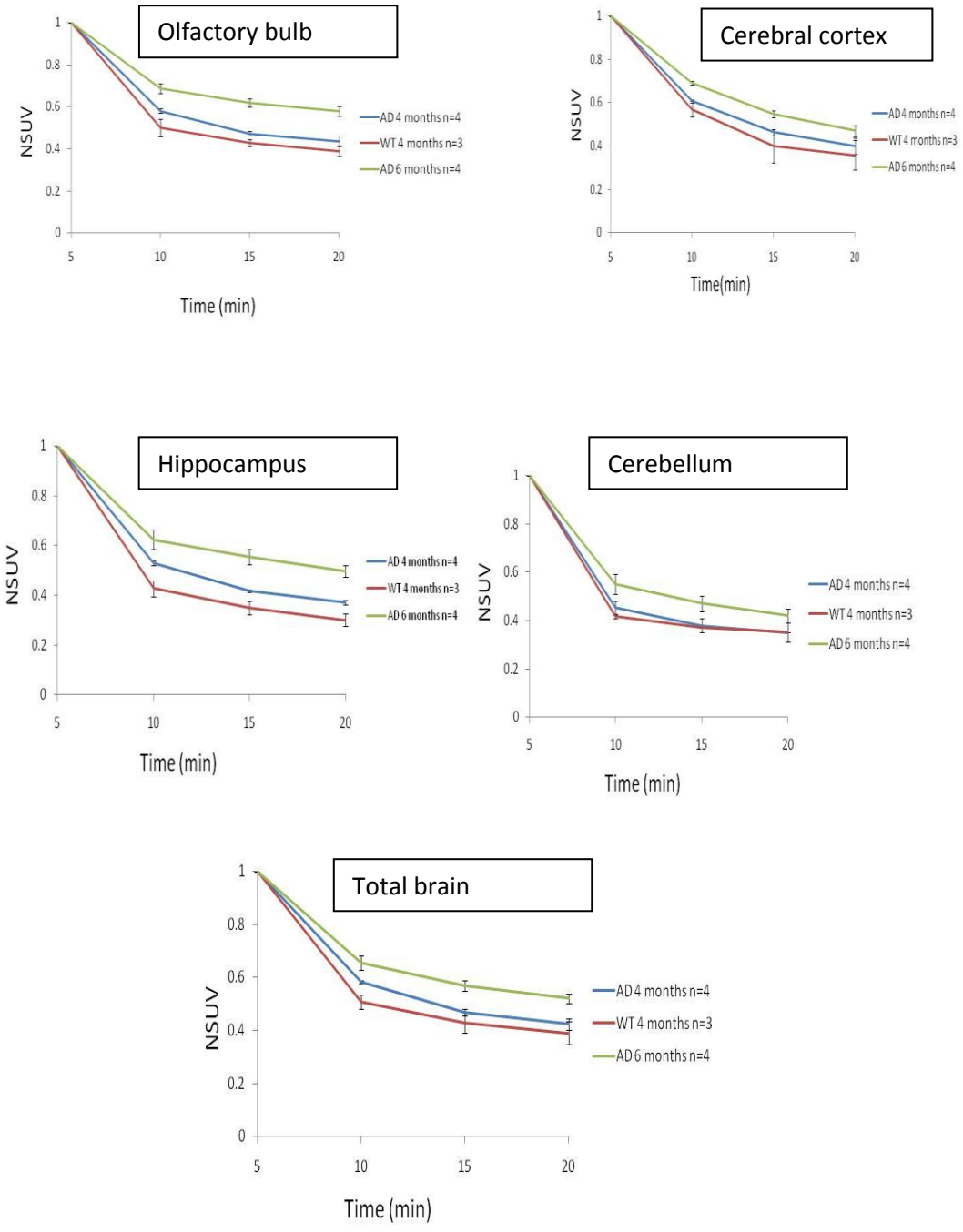

Fig. 20. Data represent mean SUV normalized to the first time point ± the SE in each region of the brain for AD and control mice as labeled in each graph.

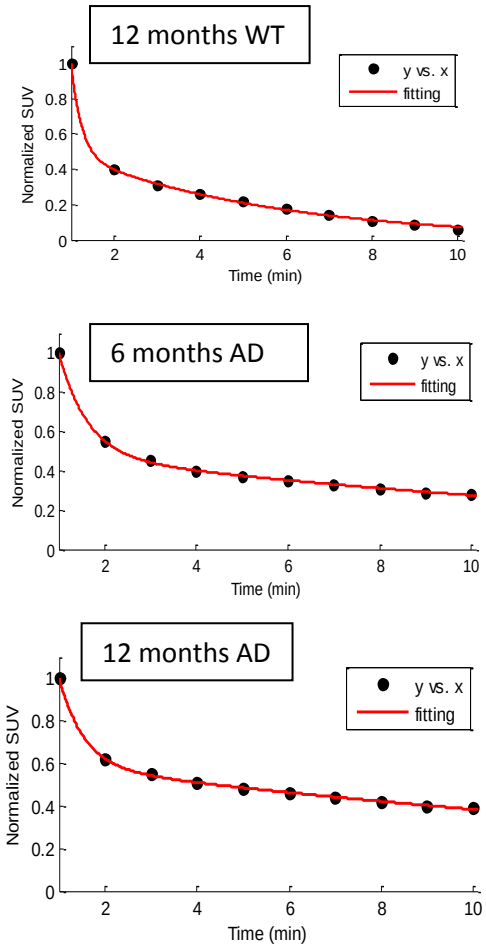

Fitting parameters	Control	6 months AD	12months AD
Fast half life (0.693/b)	0.17 min	0.4 min	0.4 min
Slow half life (0.693/d)	3.3 min	11.4 min	15.1 min

Fig. 21. Curve fitting results for total brain TACs of control mice, 6 months AD mice and 12 months AD mice.

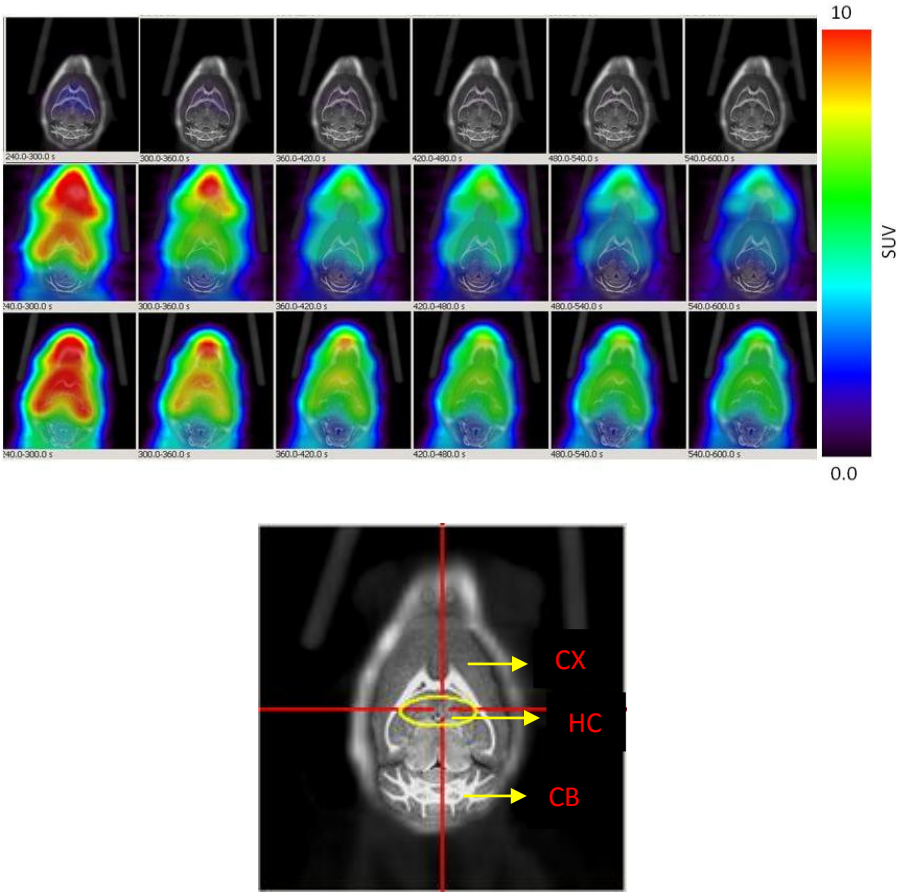

Fig. 22. Dynamic PET images (5min-10min) show the difference between brain uptakes of control (1st row: 6 images), 6 months (2nd row: 6 images) and 12 months (3rd row: 6 images) AD mice. The view is coronal section at the level of the hippocampus as indicated in the brain atlas labeled image.

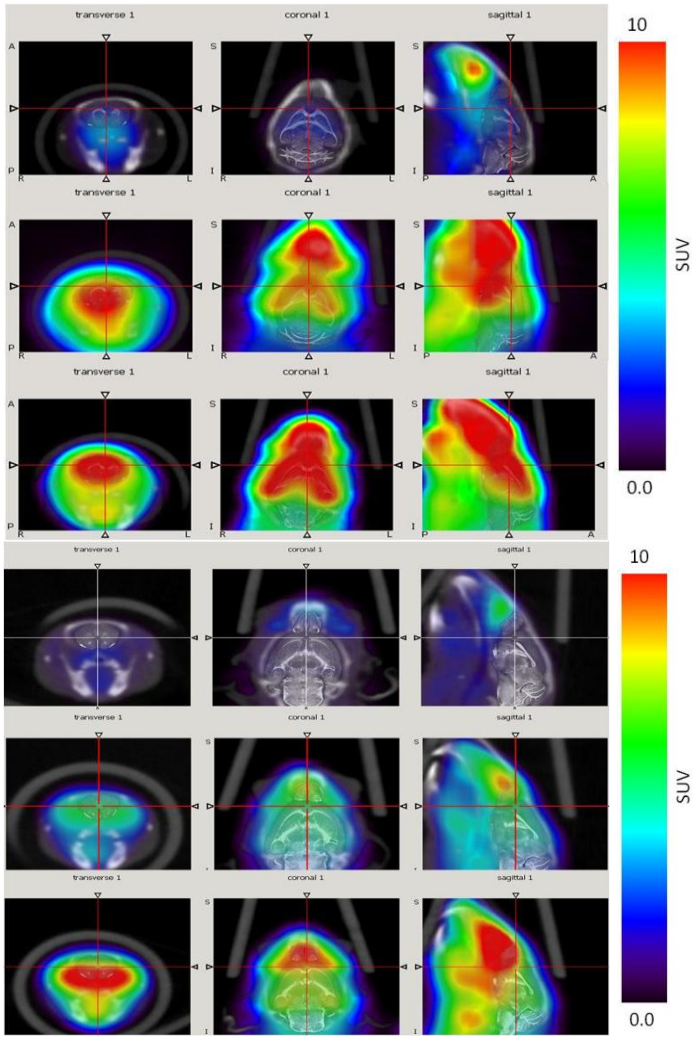

Fig. 23. Shows summed images (0-600s) of control 12months (1st row), 6 months AD (2nd row) and 12 months (3rd row) AD mice respectively in different planes as labeled in (a), and summed images (0-600s) of control 4 months (1st row), 4 months AD (2nd row) and 6 months (3rd row) AD mice respectively in different planes as labeled in (b).

5. Correlation studies

5.1. Correlation between PET and autoradiography imaging

Autoradiography images showed higher uptake for AD brain sections in comparison to control. In addition, regional analysis for autoradiography demonstrated higher activity for the cortex and the cerebellum of AD in comparison to control mice. The results reflect similar pattern as observed in the PET imaging (Fig. 24).

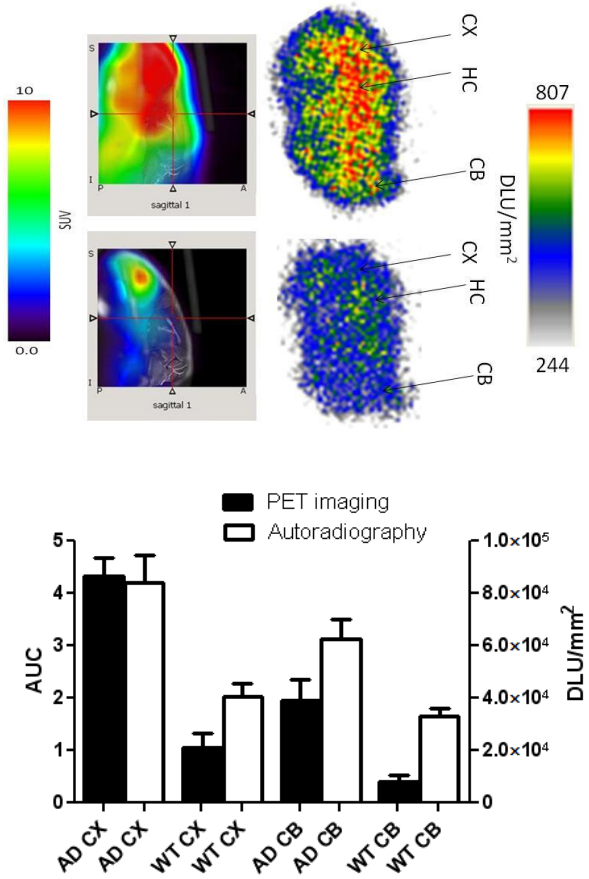

Fig. 24. Correlation between autoradiography and PET imaging in AD and control mice in the cerebellar and cortex regions.

5.2. Correlation between PET imaging and histology

Immunohistochemistry results showed variation in the plaques density in different regions of AD brain including cerebral cortex, hippocampus and the cerebellum. PET imaging showed higher uptake and histology showed higher plaque density in the cerebral cortex than the cerebellum (Fig. 25).

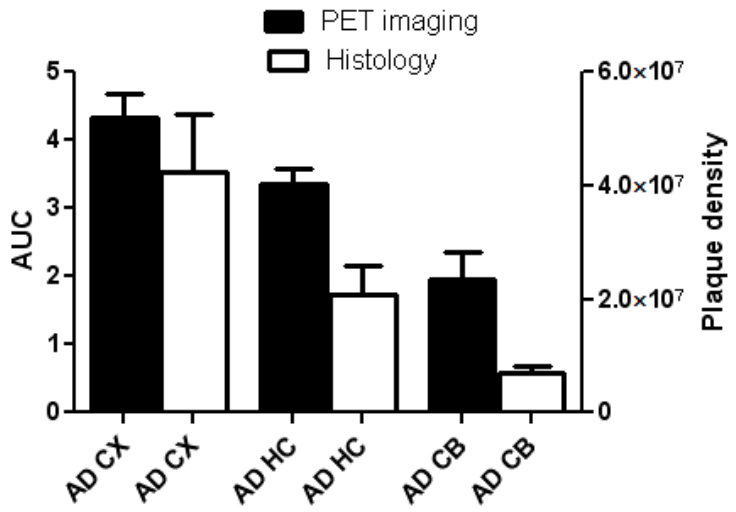

Fig. 25. Correlation between histology and PET imaging to show the variation in the uptake and plaque density in the AD brain regions including cerebral cortex, hippocampus and cerebellum.

5.3. Correlation between autoradiography imaging and histology

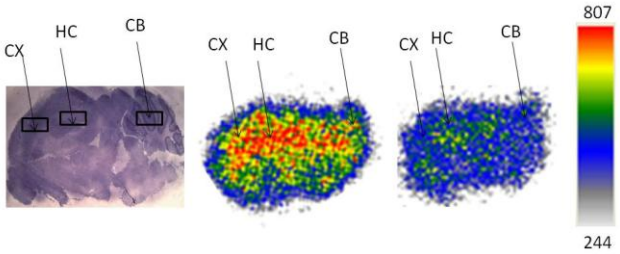

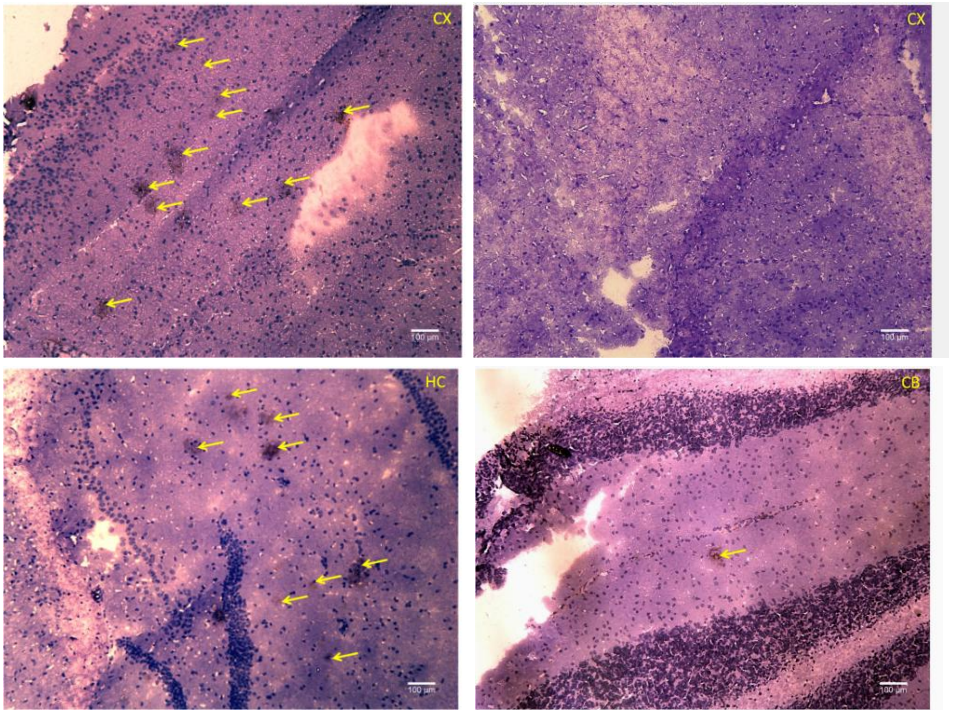

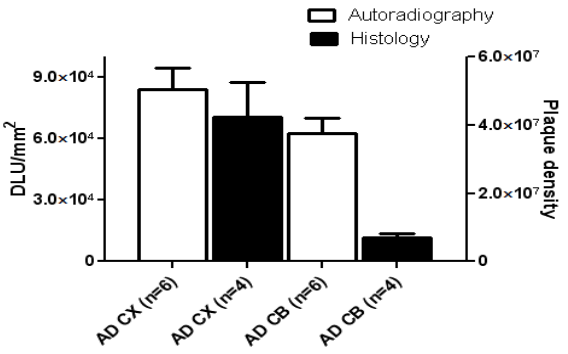

Fig. 26. Correlation between autoradiography and immunohistochemistry to show higher uptake and plaque density in the cerebral cortex than the cerebellum.

6. Biodistribution of 2-F-8-HQ in normal mice

6.1. Materials and methodology

Normal mice (n=16) were injected with 60-90µCi of 2-F-8-HQ via tail vein and 4 mice were sacrificed at different time points (2, 5, 15, and 60 min). Different organs were immediately dissected and weighted. Then, activity (CPM) of samples was measured and automatically corrected for background and decay using a gamma counter (PerkinsElmer 2480 Automatic Gamma Counter). Mouse uptake was calculated according to the following equation:

$$Uptake\ \left(\%\ dose\frac{kg}{100g}\right) = \frac{cpm\ (tissue) \times Body\ Weight\ (kg) \times 10000}{Tissue\ Weight\ (g) \times cpm(dose)}$$

The uptake values were expressed as percentage of injected dose per tissue weight multiplied by the body weight (140).

6.2. Results and discussion

Mice biodistribution data are given in table 4. We can notice the compound has fast uptake within the first 2min and rapid clearance from the brain. Most of organs have very low activity 60 min postinjection. In addition, the compound showed higher uptake (%ID/g) in the brain than our previous compound (I-125 CQ) as noticed in table 5.

Organ	**Mouse uptake (%)**			
	2 min (n=4)	5 min (n=4)	15 min (n=4)	60 min (n=4)
Lung	0.596±0.03	0.317±0.029	0.135±0.0077	0.026±0.0057
Liver	0.465±0.02	0.368±0.0282	0.110±0.0153	0.013±0.002
Spleen	0.121±0.009	0.092±0.0108	0.024±0.0051	0.005±0.0014
Kidney	1.828±0.366	1.845±0.202	0.503±0.08	0.044± 0.0083
Heart	0.212±0.0166	0.123±0.0074	0.047±0.011	0.004±0.0017
Brain	0.053±0.0023	0.032±0.0007	0.011±0.0006	0.002±0.0003
Muscle	0.067±0.006	0.055±0.014	0.049±0.0195	0.0232±0.01
Bladder	0.057±0.0340	0.078±0.049	4.072±1.7421	0
Stomach	0.137±0.011	0.093±0.014	0.059±0.0122	0.0180±0.009

Table. 4. Mice biodistribution data expressed as % $dose\frac{kg}{g}$ at different time points. The data represent the mean value ±SE.

	2 min	5 min	15 min	30 min	60 min
I-125 CQ	1 ±0.4	1 ±0.3	0.3 ±0.1	0.3 ±0.1	0.1 ±0.1
F-18 HQ	2.05±0.4	1.27±0.12	0.47±0.5	-	0.1 ±0.03

Table. 5: *In vivo* biodistribution of I-125 CQ and F-18 HQ in wild type mice (brain uptake in %ID/g $\pm$ SD).

7. Conclusions and future directions

Time activity curves (TACs) of AD mice brain showed more retention of the activity in comparison to the control mice. In addition, TACs of the 12-month AD mice demonstrated higher brain activity than the 6- and 4-month AD and the control mice. During the first 2 minutes, there was a rapid uptake of the compound. In addition, the retention of the total brain region for the older mice was significantly higher than that of the younger mice. Curve fitting of TACs for the total brain region showed longer half-life of the compound in the first and the second decay phases for the AD mice in comparison to the control.

The regional analysis of the PET images demonstrated higher uptakes in the regions associated with plaques in comparison with the normal mice, where cerebral regions have more activity than the cerebellum. Dynamic PET images demonstrated fast clearance of the compound in the normal brain and higher accumulation of the compound in the cerebral regions of the AD mice than that of the cerebellum region.

In vitro binding study results showed high affinity to Aβ-Zn with a Kd value of 1.5 nM. The fitting showed that the Hill slope value is 2.2 indicating that the receptor or ligand has multiple binding sites with positive cooperativity. The Kd value is within the range reported (0.5-3.7 nM) for previous amyloid plaques targeting agents.

Autoradiography imaging showed significant higher uptake in AD brain sections in comparison to controls. In addition, regional analysis for autoradiography demonstrated higher activity for the cortex and the cerebellum of AD in comparison to control mice. The results correlated very well with the PET imaging.

Immunohistochemistry results showed variations in the plaques density in different regions of AD brain including cerebral cortex, hippocampus and the cerebellum and the control mice had no plaques. Good correlations were found between histology, autoradiography and PET imaging.

Fluorescence imaging showed that different solvents had significant influence on the fluorescence intensity of the metal complex. The results showed no significant changes for solvents (buffers) and they were similar to the quartz slide alone. The signal intensity of 2-F-8-HQ seems to increase upon binding to zinc. In addition, HEPES buffer has shown to improve the signal intensity in comparison to the other solvents. The binding affinity saturation curve showed the maximum fluorescence intensity at (2:1) ratio (ligand to metal). Upon adding EDTA to 2-F-8-HQ–Zn, the fluorescence intensity was reduced to a level similar to the 2-F-8-HQ alone demonstrating competition in binding to zinc.

The results of the binding study strongly suggest the binding of 2-F-8-HQ to Zn. The increased fluorescence intensity at 2:1 ratio (ligand to metal) is concurrent with previous results regarding the stability of the metal complexes with a stoichiometric ratio of 2:1. Addition of EDTA (a strong chelating agent) demonstrated the inhibition of the 2-F-8-HQ–Zn formation which was indicated as a marked reduction in the fluorescence intensity to a level similar to that of 2-F-8-HQ alone.

According to the biodistribution data, we noticed the compound has fast uptake within the first 2 minutes. Most of the organs have very low activity 60 minutes postinjection.

This compound (2-F-8-HQ) has demonstrated promising results for *in vivo* imaging. The ability of detecting variation in plaque density among different AD mice ages correlated with activity uptake in the brain indicating a great role for noninvasive early detection of Alzheimer's disease in AD transgenic mice.

This may be valuable in assessing the efficacy of potential therapeutic agents. There are other animal models of Alzheimer's disease such as APOE4 model. In addition, testing other markers for AD such as over expression of tangles may provide further valuable information about the early detection of the disease progression. Furthermore, correlation with other imaging agents such as FDG may add powerful tool for disease characterization. This

compound may prove to be helpful in imaging other disease processes with elevated level of metals.

Grant support:

Worsham Fund and NIH (NIA) Grant# 1RC1AG03308

Jordan University of Science and Technology

9. Appendices

Appendix 1. Fluorescence imaging of 2-F-8-HQ in different buffers data

Time (min)	Q slide	HEPES	PBS	TRIS	2-F-8-HQ	2-F-8-HQ-Zn/Ethanol	2-F-8-HQ-Zn/HEPES	2-F-8-HQ-Zn/PBS	2-F-8-HQ-Zn/TRIS
1	0.3	0.28	1.30	0.520	78.87	18.038	818.4	86.393	166.708
2	1.66	0.77	2.61	2.84	55.97	78.759	856.2	74.33	197.163
3	2.70	0.38	1.15	2.26	28.81	145.903	913.5	76.138	216.95
4	2.05	1.06	2.71	2.53	32.12	150.132	975.4	115.606	233.213
5	2.38	2.22	2.25	2.32	46.53	153.027	1034.9	199.836	250.29
6	1.87	1.59	2.59	1.95	49.04	155.10	1097.2	315.399	264.132
7	2.42	0.78	1.74	1.73	54.16	155.37	1168.2	461.428	280.195
8	2.07	0.43	2.92	0.066	58.45	157.18	1251.7	642.907	297.99
9	2.46	0.37	2.53	0.80	64.05	157.94	1351.2	827.982	313.76
10	2.00	0.19	1.34	1.47	69.65	159.04	1463.9	969.009	332.070
Average	1.96	0.810	2.119	1.65	53.77	133.05	1093.06	376.904	255.249
SD	0.67	0.656	0.66	0.92	15.567	47.015	214.99	333.629	52.75
SE	0.21	0.20	0.21	0.29	4.922	14.86	67.98	105.502	16.68

Appendix 2. Fluorescence imaging of 2-F-8-HQ-Zn binding affinity data

[Zn]mM	[2-F-8-HQ] mM	1st exp	2nd ex	3rd exp	Average	SD	SE
3	0	0.2	0.35	0.23	0.26	0.079	0.045
3	1	45	60	59	54.66	8.386	4.841
3	1.5	102.2	161	123	128.73	29.816	17.214
3	3	210	208	218	212	5.291	3.055
3	6	333	387	369	363	27.495	15.874
3	12	308	341	269	306	36.041	20.808

Appendix 3. Fluorescence imaging of 2-F-8-HQ-Zn-EDTA competition assay data

Agents	1stexp	2ndexp	3rdexp	Average	SD	SE
EDTA	5.95	8.1	2.9	5.65	2.612	1.508
EDTA-Zn	1.2	2.8	3.6	2.53	1.222	0.705
2-F-8-HQ	195	216	231	214	18.083	10.44
2-F-8-HQ-Zn	439	461	453	451	11.135	6.429
EDTA-Zn-2-F-8-HQ	197	143	234	191.33	45.76	26.421

Appendix 4. *In vitro* binding affinity of radiolabeled 2-F-8-HQ- Aβ-Zn data

Conc nM	CPM(2-F-8-HQ + Aβ -Zn) after centrifuge					
	1st	2nd	3rd	Average	SD	SE
4.17	14563	17238	14806	15535.66	1479.262	854.052
2.085	7582	9184	10609	9125	1514.36	874.317
0.417	1416	1139	1128	1227.666	163.194	94.220
0.2385	759	1093	927	926.333	167.0009	96.418
0.0417	303	257	240	266.66	32.593	18.817
0.02085	101	187	225	171	63.529	36.678

Conc nM	CPM(2-F-8-HQ alone) after centrifuge					
	1st	2nd	3rd	Average	SD	SE
4.17	8287	9530	9196	9004.33	643.28	371.4
2.085	4700	4538	3329	4189	749.17	432.53
0.417	895	874	971	913.33	51.03	29.463
0.238	563	410	478	483.66	76.65	44.258
0.041	217	167	143	175.66	37.75	21.797
0.020	88	75	126	96.33	26.50	15.3

Appendix 5. Brain sections autoradiography quantifications data

DLU /mm2	AD	Control
	35,716	24,925
	39,551	15,399
	43,011	29,49
	30,308	26,819
	54,652	
	43,696	
	33,187	
	45,916	
	38,096	
Average	40,459	24,158
SD	6936.52	5310.785
SE	2312.175	2655.392

Appendix 6. Cerebral cortex and cerebellum autoradiography quantifications data

DLU /mm2	AD CX	WT CX	AD CB	WT CB
	117,130	48,407.	90,536	38,563
	114,260	25,087	73,616	23,660
	82,540	44,582	67,216	35,122
	68,364	43,605	51,572	34,528
	67,810		48,510	
	55,783		44,080	
Average	84,315	40,420	62,588	32,968
SD	25,758	10,430	17,811	6,455
SE	10516.057	5215.152	7271.443	3227.832

Appendix 7. Cerebral cortex plaques density quantifications data

Cortex (ROIs)	Area (pixels)	Signal intensity	Density (Area*intensity)
1	4840	149.53	
2	7352	146.02	
3	5268	147.38	
4	4416	104.29	
5	4288	114.27	
6	4020	98.53	
7	2580	93.49	
8	1040	71.26	
9	10212	107.14	
Total	44016	1031.91	45420550.56
1	6444	69.6	
2	14840	71.62	
3	38440	89.92	
4	5268	78.62	
Total	64992	309.76	20131921.92
1	2452	135.03	
2	2376	101.68	
3	3396	112.76	
4	9620	111.25	
5	1648	112.86	
6	1804	116.07	
7	4780	102.48	
8	11924	100.09	
9	2320	114.4	
10	1612	95.64	
11	6736	114.26	
12	3912	100.76	
Total	52580	1317.28	69262582.4
1	1576	81.76	
2	1260	62.36	
3	2032	76.95	
4	2832	85.38	
5	1460	106.51	
6	6004	96.14	
7	2292	80.79	
8	2912	73.19	
9	2452	96.3	

10	2052	72.79	
11	752	114.69	
12	792	88.87	
13	3440	110.87	
Total	29856	1146.6	34232889.6
Average			42261986.12
SD			20762264.34
SE			10381132.17

Appendix 8. Hippocampus plaques density quantifications data

HC (ROIs)	Area(pixels)	Signal intensity	Density (Area*intensity)
1	3382.8	92.77	
2	4069.86	72.25	
3	2590.71	47.77	
4	6787.48	63.05	
5	1973.67	114.51	
6	4463.72	78.67	
7	940.88	58.23	
Total	24209.12	527.25	12764258.52
1	2208	107.87	
2	3540	98.28	
3	7712	115.59	
4	2988	104.82	
5	1940	105.08	
6	3816	113.87	
7	1744	102.97	
8	1740	112.6	
9	1252	106.25	
10	5412	120.28	
Total	32352	1087.61	35186358.72
1	5088	113.4	
2	2216	105.56	
3	1804	97.97	
4	1292	112.4	
5	1008	119.22	
6	684	117.08	
7	1060	109.57	
8	2912	128.21	
9	4772	114.54	
Total	20836	1017.95	21210006.2
1	4080	86.08	
2	2796	98.49	
3	752	84.5	
4	3544	101.55	
5	4188	92.6	
6	928	92.54	
7	972	89.33	

8	1124	121.13	
Total	18384	766.22	14086188.48
Average			20811702.98
SD			10275914.89
SE			5137957.447

Appendix 9. Cerebellum plaques density quantifications data

CB (ROIs)	Area(pixels)	Signal intensity	Density (Area*intensity)
1	4304	89.5	
2	2740	99.87	
3	2100	79.95	
4	7748	94.75	
5	4632	84.92	
Total	21524	448.99	9664060.76
1	3228	86.1	
2	3212	100.35	
3	5284	91.47	
4	3532	86.89	
Total	15256	364.81	5565541.36
1	3308	89.21	
2	2452	94.12	
3	1804	106.62	
4	4328	63.16	
5	980	113.69	
6	2644	87.64	
Total	15516	554.44	8602691.04
1	2563.55	119.72	
2	2182.99	98.54	
3	8547.94	113.76	
Total	13294.48	332.02	4414033.25
Average			7061581.602
SD			2476258.249
SE			1238129.125

Appendix 10. Radiation dosimetry estimation

Background

Hydroxy quinoline derivatives have shown the potential as therapeutic agents for treating Alzheimer disease (138). In addition to the therapeutic effect, we have investigated the feasibility of imaging AD mice using radiolabeled hydroxy quinoline (2-F-8-HQ) and showed promising results in comparison to control mice (139). The aim of this study is to estimate the radiation dose of this compound in human based on mice biodistribution data.

Materials and methodology

Normal mice (n=16) were injected with 60-90µCi of 2-F-8-HQ via tail vein and 4 mice were sacrificed at different time points (2-5-15-60min). Different organs were immediately dissected and the weight of each organ was calculated. Then, activity of samples (CPM) was measured and automatically corrected for background and decay using a gamma counter (PerkinsElmer 2480 Automatic Gamma Counter). Mouse uptake was calculated according to the following equation:

$$Uptake\left(\%\, dose\,\frac{kg}{100g}\right) = \frac{cpm\,(tissue) \times Body\ Weight\,(kg) \times 10000}{Tissue\ Weight\,(g) \times cpm(dose)}$$

The uptake values were expressed as percentage of injected dose per tissue weight multiplied by the body weight, cpm: counts per minute (140)

After calculating mice uptake, data were converted to human data (141) by multiplying to the corresponding human tissue (150) and dividing by the reference man weight (70kg).

$$\frac{Mice\ uptake\left(\%\frac{kg\ dose}{g}\right)\times Human\ tissue\ weight\ (g)}{Standard\ human\ body\ weight\ (70kg)}$$

Human time activity curves (TACs) of most organs were best fitted into two phase decay equation except for bladder and kidney where the best fitting was found in other equations using XLfit® software (Fig. 27).

$$A\times\exp(-B\times x)+C\times\exp\left(-D\times x\right)$$

$$\exp\left(\left(A+\left(\frac{B}{x}\right)\right)+\left(C\times In(x)\right)\right)\text{ (Bladder fitting equation)}$$

$$\left(A+\left(\frac{B}{1+\exp\left(\left(\left((-1)\times C\right)+\left(D\times In(x)\right)\right)+\left(E\times x\right)\right)}\right)\right)\text{ (Kidney fitting equation)}$$

Residence activity time (τ) was calculated as the time integral of the fraction of administered activity for each organ (142). Hence, area under curve (AUC) of TACs was calculated and expressed as percentage of injected dose multiplied by time (min) and then converted to hour unit.

$$\tau=\int_0^x\frac{A(t)}{A_0}dt$$

The cumulated activity ($\tilde{A}_h$) of 1 MBq for each organ in the reference man (70kg) was calculated by multiplying the residence time of TAC by 1 MBq as an injected dose in the reference man (141).

$$\tilde{A}_h = 1MBq \times \tau = 1MBq \times \int_0^x \frac{A(t)}{A0} dt$$

The cumulated activity for the remainder of the body ($\tilde{A}_{rb}$) was calculated as the difference between the cumulated activity in the total body ($\tilde{A}_{tb}$) and the sum of cumulated activities of source organs ($\tilde{A}_{hi}$) (143).

$$\tilde{A}_{rb} = \tilde{A}_{tb} - \sum_i \tilde{A}_{hi}$$

Mean absorbed dose for each target organ was calculated by using tabulated S values for F-18 (144, 145). In addition, S values form brain and heart as source organs (r_h) to different targets (r_k) were calculated from reported specific absorbed fractions (Φ_i) (146, 147), the decay scheme and the mean energy emitted per nuclear transition (Δ_i) data of F-18 (148). Both positron and gamma photon were used as penetrating radiation for S values calculation because of their high energy and mouse organs are very small in comparison to human (149) (Table. 6).

$$S(r_k \leftarrow r_h) = \sum_i \Delta_i \Phi_i(r_k \leftarrow r_h)$$

The S values from the remainder of the body to target organs were calculated as the following:

$$S(r_k \leftarrow rb) = S(r_k \leftarrow tb)\frac{m_{tb}}{m_{rb}} - \sum_h S(r_k \leftarrow r_h)\frac{m_h}{m_{rb}}$$

The unit of S is RAD/μCi-h, m_h is the source organ mass (g), m_{rb} is the remainder body weight (g) which calculated by subtracting the total body weight (m_{tb}) from the total mass of source organs (149).

The mean dose to the target organs (D_k) were calculated by the following equation (141):

$$D_k = \sum_h \left[\tilde{A}_h\, S(r_k \leftarrow r_h)\right] + \tilde{A}_{rb}\, S(r_k \leftarrow rb)$$

The effective dose (E, unit: Sv) was calculated by multiplying the mean absorbed dose (equivalent to H_k) of each target organ to the corresponding tissue weighting factor (W_k) (151), other unspecified organs were assumed to have the same dose as the total body (141).

$$E = \sum^{k} W_k\, H_k$$

Results and discussion

Mice and equivalent human biodistribution data are given in table 4 and 7. We can notice the compound has fast uptake within the first 2 minutes and rapid clearance from the body. Most of the organs have very low activity 60 min postinjection. Based on the weight of each organ in reference human, a maximum of 27% uptake within the first 2 minutes was observed in the muscle followed by the liver (12%).

Cumulated activities results showed very low activities in most of the organs (Table 8). The maximum cumulated activity occurred in the muscle (1.54E-1) followed by the bladder (3.9E-2). The minimum cumulated activity occurred in the spleen (5.17E-4). Mean absorbed dose (mGy/MBq) results showed the maximum dose in the bladder followed by the kidney and the minimum was found in the brain (Table. 9).The effective dose was found to be about 4.48E-3 mSv/MBq (Table. 9).

Dosimetry estimation of this compound has never been reported before. This compound has shown promising results in our initial imaging studies. Biodistribution results showed rapid uptake and fast clearance from normal tissues. The estimated effective dose (4.48E-3 mSv/MBq) was found to be within the safe dose limit determined by FDA (0.03Sv); 370MBq of 2-F-8-HQ will result in about 1.7 mSv (141, 152, 153). The results were similar to the estimated dosimetry of FET (oncologic PET tracer) where the effective

dose was found to be about 9E-3mSv/MBq. Although the activity was measured up to 60 minutes (considered as short time), the compound demonstrated rapid clearance. In addition, bladder activity was considered in this study without taking voiding and tracer excretion into account which can affect the dose to the bladder and the other organs (141).

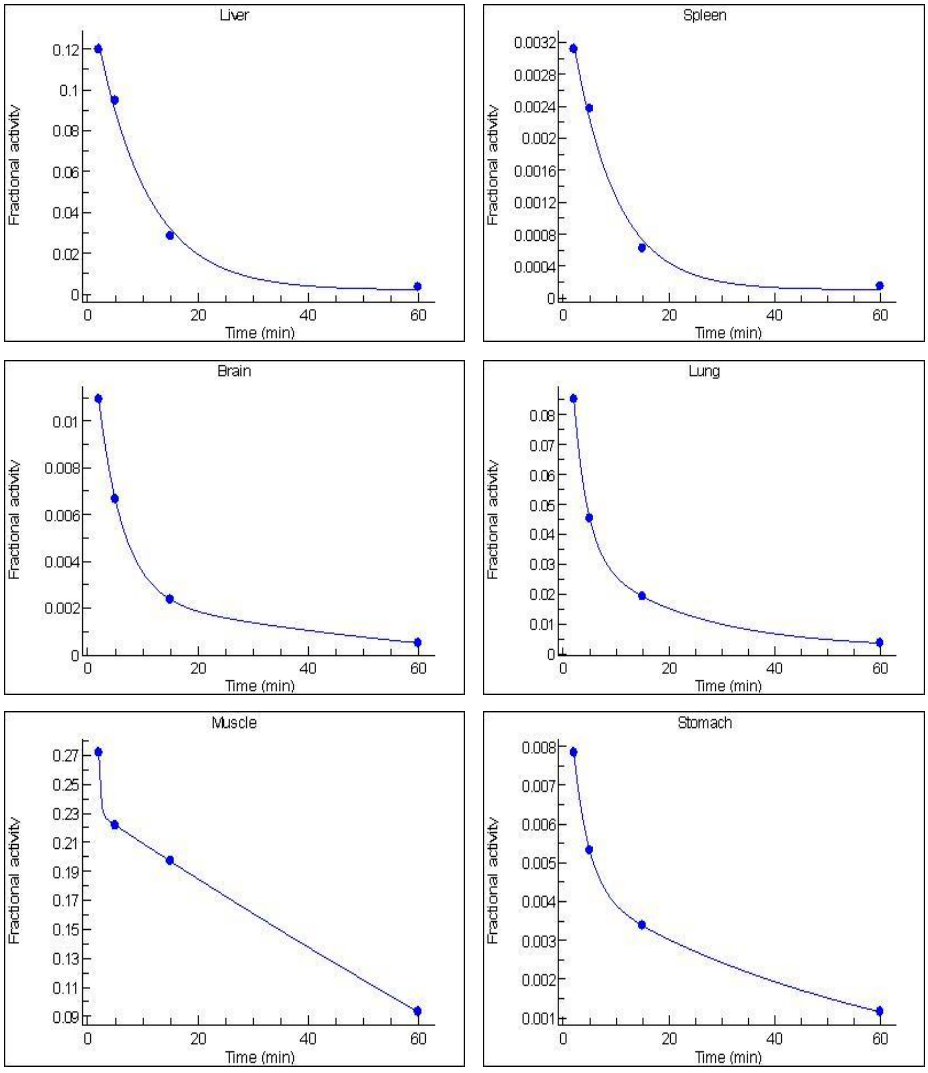
Liver
Fractional activity
0.12
0.1
0.08
0.06
0.04
0.02
0
0
20
40
60
Time (min)
Spleen
Fractional activity
0.0032
0.0028
0.0024
0.002
0.0016
0.0012
0.0008
0.0004
0
0
20
40
60
Time (min)
Brain
Fractional activity
0.01
0.008
0.006
0.004
0.002
0
0
20
40
60
Time (min)
Lung
Fractional activity
0.08
0.07
0.06
0.05
0.04
0.03
0.02
0.01
0
0
20
40
60
Time (min)
Muscle
Fractional activity
0.27
0.25
0.23
0.21
0.19
0.17
0.15
0.13
0.11
0.09
0
20
40
60
Time (min)
Stomach
Fractional activity
0.008
0.007
0.006
0.005
0.004
0.003
0.002
0.001
0
20
40
60
Time (min)

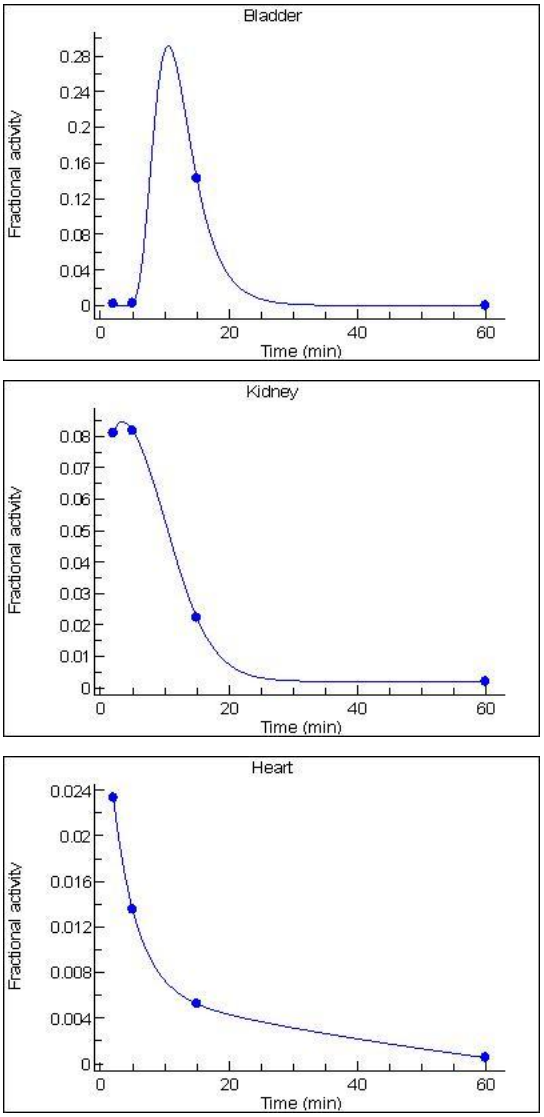

Fig. 27. Time activity curves (TACs) of fractional activity for human organs as labeled in each graph.

Target organ	Source organ										
	Lung	Liver	Spleen	Stomach	Kidney	Heart	Muscle	Bladder	Total body	Brain	Remainder of body
Lung	6.20E-04	1.70E-05	1.60E-05	1.40E-05	6.90E-06	5.49E-05	9.70E-06	3.60E-07	1.90E-05	1.56388E-06	9.83E-06
Liver	1.70E-05	4.70E-04	7.80E-06	1.50E-05	2.90E-05	2.58E-05	8.10E-06	2.10E-06	2.00E-05	2.6906E-07	3.03E-05
Spleen	1.50E-05	7.30E-06	3.80E-03	6.90E-05	6.00E-05	1.49E-05	1.10E-05	1.70E-06	2.00E-05	2.882E-07	8.96E-06
Kidney	7.60E-06	2.70E-05	6.20E-05	2.40E-05	2.20E-03	9.80E-06	1.00E-05	2.80E-06	2.00E-05	7.1784E-08	9.83E-06
Heart	5.21E-05	0.000027652	1.91968E-05	0.000029832	1.00876E-05	3.56E-04	1.16616E-05	4.8336E-07	0.000016054	7.4976E-07	1.17E-05
Brain	1.56388E-06	2.6906E-07	2.882E-07	1.65692E-07	7.1784E-08	7.88E-07	3.2012E-06	6.40724E-09	1.11192E-05	1.00222E-05	1.87E-05
Muscle	9.70E-06	8.10E-06	1.10E-05	1.00E-05	1.00E-05	1.80E-05	2.90E-05	1.30E-05	1.80E-05	3.2012E-06	1.10E-05
Bladder	5.40E-07	2.50E-06	9.90E-07	3.30E-06	2.80E-06	8.86E-07	1.30E-05	1.80E-03	2.10E-05	6.41256E-09	1.83E-05
Stomach	1.30E-05	1.40E-05	7.10E-05	1.40E-03	2.40E-05	2.02E-05	1.00E-05	2.40E-06	2.00E-05	1.34368E-07	9.81E-06
Total body	1.80E-05	2.00E-05	2.00E-05	1.50E-05	2.00E-05	1.62E-05	1.80E-05	1.40E-05	1.80E-05	1.11192E-05	1.82E-05

Table. 6. S values used to calculate the mean absorbed dose for each target organ.

Organ	Human uptake (%)			
	2 min (n=4)	5 min (n=4)	15 min (n=4)	60 min (n=4)
Lung	8.520±0.469	4.541±0.423	1.93±0.111	0.372±0.082
Liver	11.975±0.660	9.466±0.726	2.84±0.395	0.352±0.075
Spleen	0.311±0.025	0.237±0.027	0.062±0.013	0.0152±0.003
Kidney	8.096±1.624	8.174±0.896	2.22±0.354	0.197±0.036
Heart	2.334±0.183	1.355±0.081	0.526±0.128	0.053±0.018
Brain	1.092±0.047	0.666±0.0142	0.237±0.013	0.051±0.008
Muscle	27.189±2.616	22.16±5.712	19.724±7.838	9.313±4.055
Bladder	0.202±0.119	0.274±0.173	14.25±6.097	0
Stomach	0.784±0.067	0.532±0.08	0.338±0.07	0.116±0.051

Table. 7. Human biodistribution data expressed as $\%\,dose$ at different time points. The data represent the mean value ±SE.

Organ	Cumulated activity of 1MBq (MBq.h)
Lung	1.43E-02
Liver	2.07E-02
Spleen	5.17E-04
Kidney	1.70E-02
Heart	4.00E-03
Brain	1.83E-03
Muscle	1.54E-01
Bladder	3.90E-02
Stomach	2.50E-03
Total body	1.66E-01

Table. 8. Cumulated activities in different organs calculated as the integral of the fractional activity and multiplied by 1MBq injected dose in the reference human (70kg).

Target organ	Absorbed dose (mGy/MBq)
Lung	4.09E-03
Liver	4.85E-03
Spleen	2.56E-03
Kidney	1.19E-02
Heart	2.30E-03
Brain	1.09E-03
Muscle	2.57E-03
Bladder	2.09E-02
Stomach	2.79E-03
Total body	2.45E-03
Effective dose (mSv/MBq)	4.48E-03

Table. 9. Mean absorbed dose (mGy/MBq) for each target organ and the total effective dose (mSv/MBq).

Bibliography

1. STELZMA RAINULF , S. N., MURllAGH F An English translation of Alzheimer's 1907 Paper, "Uber eine eigenartige Erkankung der Hirnrinde". *Clinical Anatomy* **8**, 429-431 (1995).

2. Castellani Rudy, R. R., Smith Mark. Alzheimer Disease. *Dis Mon* **56**, 484-546 (2010).

3. Carter, M. D., Simms, G. A. & Weaver, D. F. The Development of New Therapeutics for Alzheimer's Disease. *Clin Pharmacol Ther* **88**, 475-486 (2010).

4. Wollen, K. Alzheimer's disease: the pros and cons of pharmaceutical, nutritional, botanical, and stimulatory therapies, with a discussion of treatment strategies from the perspective of patients and practitioners. *Altern Med Rev* **15**, 223-244 (2010).

5. Kadir, A. & Nordberg, A. Target-Specific PET Probes for Neurodegenerative Disorders Related to Dementia. *Journal of Nuclear Medicine* **51**, 1418-1430, doi:10.2967/jnumed.110.077164 (2010).

6. Perrin, R. J., Fagan, A. M. & Holtzman, D. M. Multimodal techniques for diagnosis and prognosis of Alzheimer's disease. *Nature* **461**, 916-922 (2009).

7. Lippa, C. F. *et al.* Familial and sporadic Alzheimer's disease. *Neurology* **46**, 406-412 (1996).

8. Bird, T. D. Alzheimer Overview. *GeneClinics*, 13-16 (2001).

9. Xiong L. , G. C., Roulea G. A. . Genetics of Alzheimer's Disease and Research Frontiers in Dementia. *Geriatrics and Aging* **8**, 31-35 (2005).

10. Stanton, L. R. & Coetzee, R. H. Down's syndrome and dementia. *Adv Psychiatr Treat* **10**, 50-58, doi:10.1192/apt.10.1.50 (2004).

11. Menéndez, M. Down syndrome, Alzheimer's disease and seizures. *Brain and Development* **27**, 246-252 (2005).

12. Gauthier, S. *et al.* Mild cognitive impairment. *The Lancet* **367**, 1262-1270 (2006).

13. Winblad, B. *et al.* Mild cognitive impairment – beyond controversies, towards a consensus: report of the International Working Group on Mild Cognitive Impairment. *Journal of Internal Medicine* **256**, 240-246, doi:10.1111/j.1365-2796.2004.01380.x (2004).

14. Ganguli, M., Dodge, H. H., Shen, C. & DeKosky, S. T. Mild cognitive impairment, amnestic type. *Neurology* **63**, 115-121, doi:10.1212/01.wnl.0000132523.27540.81 (2004).

15. Association, A. s. Alzheimer's Disease Facts and Figures *Alzheimer's & Dementia* **6** (2010).

16. Weiner, M. W. *et al.* The Alzheimer's Disease Neuroimaging Initiative: Progress report and future plans. *Alzheimer's and Dementia* **6**, 202-211.e207 (2010).

17. Hebert, L. E., Scherr, P. A., Bienias, J. L., Bennett, D. A. & Evans, D. A. Alzheimer Disease in the US Population: Prevalence Estimates Using the 2000 Census. *Arch Neurol* **60**, 1119-1122, doi:10.1001/archneur.60.8.1119 (2003).

18. Plassman, B. L. *et al.* Prevalence of Dementia in the United States: The Aging, Demographics, and Memory Study. *Neuroepidemiology* **29**, 125-132 (2007).

19. Hebert, L. E., Beckett, L. A., Scherr, P. A. & Evans, D. A. Annual Incidence of Alzheimer Disease in the United States Projected to the Years 2000 Through 2050. *Alzheimer Disease & Associated Disorders* **15**, 169-173 (2001).

20. Larson, E. B. *et al.* Survival after Initial Diagnosis of Alzheimer Disease. *Annals of Internal Medicine* **140**, 501-509 (2004).

21. Castellani, R. J., Rolston, R. K. & Smith, M. A. Alzheimer Disease. *Disease-a-Month* **56**, 484-546 (2010).

22. Probst, A., Brunnschweiler, H., Lautenschlager, C. & Ulrich, J. A special type of senile plaque, possibly an initial stage. *Acta Neuropathologica* **74**, 133-141, doi:10.1007/bf00692843 (1987).

23. Miyawaki, K., Nakayama, H., Nakamura, S.-i., Uchida, K. & Doi, K. Three-dimensional structures of canine senile plaques. *Acta Neuropathologica* **102**, 321-328, doi:10.1007/s004010000354 (2001).

24. Mattiace, L. A., Davies, P., Yen, S. H. & Dickson, D. W. Microglia in cerebellar plaques in Alzheimer's disease. *Acta Neuropathologica* **80**, 493-498, doi:10.1007/bf00294609 (1990).

25. Haga, S., Akai, K. & Ishii, T. Demonstration of microglial cells in and around senile (neuritic) plaques in the Alzheimer brain. *Acta Neuropathologica* **77**, 569-575, doi:10.1007/bf00687883 (1989).

26. Attems, J., Lintner, F. & Jellinger, K. Amyloid ß peptide 1–42 highly correlates with capillary cerebral amyloid angiopathy and Alzheimer disease pathology. *Acta Neuropathologica* **107**, 283-291, doi:10.1007/s00401-004-0822-6 (2004).

27. Knudsen, K. A., Rosand, J., Karluk, D. & Greenberg, S. M. Clinical diagnosis of cerebral amyloid angiopathy: Validation of the Boston Criteria. *Neurology* **56**, 537-539 (2001).

28. Mann, D. *et al.* Microglial cells and amyloid β protein (Aβ) deposition: association with Aβ₄₀-plaques. *Acta Neuropathologica* **90**, 472-477, doi:10.1007/bf00294808 (1995).

29. Fukatsu, R. *et al.* Ultrastructural analysis of neurofibrillary tangles of Alzheimer's disease using computerized digital processing. *Acta Neuropathologica* **75**, 519-522, doi:10.1007/bf00687141 (1988).

30. Kawasaki, H., Murayama, S., Tomonaga, M., Izumiyama, N. & Shimada, H. Neurofibrillary tangles in human upper cervical ganglia. *Acta Neuropathologica* **75**, 156-159, doi:10.1007/bf00687076 (1987).

31. Braak, H. & Braak, E. Development of Alzheimer-related neurofibrillary changes in the neocortex inversely recapitulates cortical myelogenesis. *Acta Neuropathologica* **92**, 197-201, doi:10.1007/s004010050508 (1996).

32. Brion, J.-P. in *Alzheimer: 100 Years and Beyond Research and Perspectives in Alzheimer's Disease* eds Mathias Jucker *et al.*) 307-312 (Springer Berlin Heidelberg, 2006).

33. Lei, P. *et al.* Tau protein: Relevance to Parkinson's disease. *The International Journal of Biochemistry & Cell Biology* **42**, 1775-1778 (2010).

34. Lee, V. M.-Y., Goedert, M. & Trojanowski, J. Q. NEURODEGENERATIVE TAUOPATHIES. *Annual Review of Neuroscience* **24**, 1121-1159, doi:doi:10.1146/annurev.neuro.24.1.1121 (2001).

35. Spires-Jones, T. L., Stoothoff, W. H., de Calignon, A., Jones, P. B. & Hyman, B. T. Tau pathophysiology in neurodegeneration: a tangled issue. *Trends in Neurosciences* **32**, 150-159 (2009).

36. Zhang, Y.-w., Thompson, R., Zhang, H. & Xu, H. APP processing in Alzheimer's disease. *Molecular Brain* **4**, 3 (2011).

37. Bordji, K., Becerril-Ortega, J., Nicole, O. & Buisson, A. Activation of Extrasynaptic, But Not Synaptic, NMDA Receptors Modifies Amyloid Precursor Protein Expression Pattern and Increases Amyloid-beta Production. *J. Neurosci.* **30**, 15927-15942, doi:10.1523/jneurosci.3021-10.2010 (2010).

38. Zheng, H. & Koo, E. The amyloid precursor protein: beyond amyloid. *Molecular Neurodegeneration* **1**, 5 (2006).

39. Xu, H. *et al.* Generation of Alzheimer β-amyloid protein in the trans-Golgi network in the apparent absence of vesicle formation. *Proceedings of the National Academy of Sciences* **94**, 3748-3752 (1997).

40. Glenner, G. G. & Wong, C. W. Alzheimer's disease: Initial report of the purification and characterization of a novel cerebrovascular amyloid protein. *Biochemical and Biophysical Research Communications* **120**, 885-890 (1984).

41. Glenner, G. G. & Wong, C. W. Alzheimer's disease and Down's syndrome: Sharing of a unique cerebrovascular amyloid fibril protein.

Biochemical and Biophysical Research Communications **122**, 1131-1135 (1984).

42. Hardy, J. Framing [beta]-amyloid. *Nat Genet* **1**, 233-234 (1992).

43. Cai, X., Golde, T. & Younkin, S. Release of excess amyloid beta protein from a mutant amyloid beta protein precursor. *Science* **259**, 514-516, doi:10.1126/science.8424174 (1993).

44. Hardy, J. & Higgins, G. Alzheimer's disease: the amyloid cascade hypothesis. *Science* **256**, 184-185, doi:10.1126/science.1566067 (1992).

45. Scheuner, D. *et al.* Secreted amyloid [beta]-protein similar to that in the senile plaques of Alzheimer's disease is increased *in vivo* by the presenilin 1 and 2 and APP mutations linked to familial Alzheimer's disease. *Nat Med* **2**, 864-870 (1996).

46. Hardy, J. & Selkoe, D. J. The Amyloid Hypothesis of Alzheimer's Disease: Progress and Problems on the Road to Therapeutics. *Science* **297**, 353-356, doi:10.1126/science.1072994 (2002).

47. de la Torre, J. C. Is Alzheimer's disease a neurodegenerative or a vascular disorder? Data, dogma, and dialectics. *The Lancet Neurology* **3**, 184-190 (2004).

48. Roy, S. & Rauk, A. Alzheimer's disease and the [`]ABSENT' hypothesis: mechanism for amyloid [beta] endothelial and neuronal toxicity. *Medical Hypotheses* **65**, 123-137 (2005).

49. Bush, A. I. & Tanzi, R. E. Therapeutics for Alzheimer's Disease Based on the Metal Hypothesis. *Neurotherapeutics* **5**, 421-432 (2008).

50. Bush, A. *et al.* Rapid induction of Alzheimer A beta amyloid formation by zinc. *Science* **265**, 1464-1467, doi:10.1126/science.8073293 (1994).

51. Atwood, C. S. *et al.* Dramatic Aggregation of Alzheimer Aβ by Cu(II) Is Induced by Conditions Representing Physiological Acidosis. *Journal of Biological Chemistry* **273**, 12817-12826, doi:10.1074/jbc.273.21.12817 (1998).

52. Moir, R. D. *et al.* Differential Effects of Apolipoprotein E Isoforms on Metal-Induced Aggregation of Aβ Using Physiological Concentrations†. *Biochemistry* **38**, 4595-4603, doi:10.1021/bi982437d (1999).

53. Barnham, K. J. *et al.* Tyrosine gated electron transfer is key to the toxic mechanism of Alzheimer's disease β-amyloid. *The FASEB Journal*, doi:10.1096/fj.04-1890fje (2004).

54. Puglielli, L. *et al.* Alzheimer disease β-amyloid activity mimics cholesterol oxidase. *The Journal of Clinical Investigation* **115**, 2556-2563 (2005).

55. Huang, X. *et al.* Cu(II) Potentiation of Alzheimer Aβ Neurotoxicity. *Journal of Biological Chemistry* **274**, 37111-37116, doi:10.1074/jbc.274.52.37111 (1999).

56. Lovell, M. A., Robertson, J. D., Teesdale, W. J., Campbell, J. L. & Markesbery, W. R. Copper, iron and zinc in Alzheimer's disease senile plaques. *Journal of the Neurological Sciences* **158**, 47-52 (1998).

57. Frederickson, C. J. *et al.* Synaptic release of zinc from brain slices: Factors governing release, imaging, and accurate calculation of concentration. *Journal of Neuroscience Methods* **154**, 19-29 (2006).

58. Schlief, M. L., Craig, A. M. & Gitlin, J. D. NMDA receptor activation mediates copper homeostasis in hippocampal neurons. *J. Neurosci.* **25**, 239-246, doi:10.1523/jneurosci.3699-04.2005 (2005).

59. Uchida, Y., Takio, K., Titani, K., Ihara, Y. & Tomonaga, M. The growth inhibitory factor that is deficient in the Alzheimer's disease brain is a 68 amino acid metallothionein-like protein. *Neuron* **7**, 337-347 (1991).

60. Budimir, A. Metal ions, Alzheimer's disease and chelation therapy. *Acta Pharmaceutica* **61**, 1-14 (2011).

61. McLachlan, D. R. C. *et al.* Intramuscular desferrioxamine in patients with Alzheimer's disease. *The Lancet* **337**, 1304-1308 (1991).

62. Lee, J.-Y., Friedman, J. E., Angel, I., Kozak, A. & Koh, J.-Y. The lipophilic metal chelator DP-109 reduces amyloid pathology in brains of

human [beta]-amyloid precursor protein transgenic mice. *Neurobiology of Aging* **25**, 1315-1321.

63. Dedeoglu, A. *et al.* Preliminary studies of a novel bifunctional metal chelator targeting Alzheimer's amyloidogenesis. *Experimental Gerontology* **39**, 1641-1649.

64. Cherny, R. A. *et al.* Treatment with a Copper-Zinc Chelator Markedly and Rapidly Inhibits [beta]-Amyloid Accumulation in Alzheimer's Disease Transgenic Mice. *Neuron* **30**, 665-676 (2001).

65. Ritchie, C. W. *et al.* Metal-Protein Attenuation With Iodochlorhydroxyquin (Clioquinol) Targeting A{beta} Amyloid Deposition and Toxicity in Alzheimer Disease: A Pilot Phase 2 Clinical Trial. *Arch Neurol* **60**, 1685-1691, doi:10.1001/archneur.60.12.1685 (2003).

66. Pepeu, G. Overview and perspective on the therapy of alzheimer's disease from a preclinical viewpoint. *Progress in Neuro-Psychopharmacology and Biological Psychiatry* **25**, 193-209 (2001).

67. DRACHMAN, D. A. Memory and cognitive function in man. *Neurology* **27**, 783 (1977).

68. Lin, L., Georgievska, B., Mattsson, A. & Isacson, O. Cognitive changes and modified processing of amyloid precursor protein in the cortical and hippocampal system after cholinergic synapse loss and muscarinic receptor activation. *Proceedings of the National Academy of Sciences* **96**, 12108-12113, doi:10.1073/pnas.96.21.12108 (1999).

69. Abe, E., Casamenti, F., Giovannelli, L., Scali, C. & Pepeu, G. Administration of amyloid [beta]-peptides into the medial septum of rats decreases acetylcholine release from hippocampus *in vivo*. *Brain Research* **636**, 162-164 (1994).

70. Giovannelli, L., Casamenti, F., Scali, C., Bartolini, L. & Pepeu, G. Differential effects of amyloid peptides [beta]-(1-40) and [beta]-(25-35) injections into the rat nucleus basalis. *Neuroscience* **66**, 781-792 (1995).

71. Adessi, C. & Soto, C. Beta-sheet breaker strategy for the treatment of Alzheimer's disease. *Drug Development Research* **56**, 184-193, doi:10.1002/ddr.10074 (2002).

72. Vickers, J. C. *et al.* The cause of neuronal degeneration in Alzheimer's disease. *Progress in Neurobiology* **60**, 139-165 (2000).

73. Bales, K. R. *et al.* Apolipoprotein E is essential for amyloid deposition in the APPV717F transgenic mouse model of Alzheimer's disease. *Proceedings of the National Academy of Sciences* **96**, 15233-15238, doi:10.1073/pnas.96.26.15233 (1999).

74. Mesulam, M. M. Neuroplasticity Failure in Alzheimer's Disease: Bridging the Gap between Plaques and Tangles. *Neuron* **24**, 521-529 (1999).

75. Janus, C. & Westaway, D. Transgenic mouse models of Alzheimer's disease. *Physiology & Behavior* **73**, 873-886 (2001).

76. Wisniewski, T. & Sigurdsson, E. M. Murine models of Alzheimer's disease and their use in developing immunotherapies. *Biochimica et Biophysica Acta (BBA) - Molecular Basis of Disease* **1802**, 847-859 (2010).

77. Scali, C. *et al.* [beta](1-40) Amyloid peptide injection into the nucleus basalis of rats induces microglia reaction and enhances cortical [gamma]-aminobutyric acid release *in vivo*. *Brain Research* **831**, 319-321 (1999).

78. Aisen, P. S. *et al.* A randomized controlled trial of prednisone in Alzheimer’s disease. *Neurology* **54**, 588 (2000).

79. Ballard, C. *et al.* Alzheimer's disease. *The Lancet* **377**, 1019-1031 (2011).

80. Jack Jr, C. R. *et al.* Introduction to the recommendations from the National Institute on Aging-Alzheimer's Association workgroups on diagnostic guidelines for Alzheimer's disease. *Alzheimer's and Dementia* **7**, 257-262 (2011).

81. Rusinek, H. *et al.* Alzheimer disease: measuring loss of cerebral gray matter with MR imaging. *Radiology* **178**, 109-114 (1991).

82. Misra, C., Fan, Y. & Davatzikos, C. Baseline and longitudinal patterns of brain atrophy in MCI patients, and their use in prediction of short-term conversion to AD: Results from ADNI. *NeuroImage* **44**, 1415-1422 (2009).

83. Whitwell, J. L. & Jack Jr, C. R. Neuroimaging in Dementia. *Neurologic Clinics* **25**, 843-857 (2007).

84. Zhang, Y. *et al.* Diffusion tensor imaging of cingulum fibers in mild cognitive impairment and Alzheimer disease. *Neurology* **68**, 13-19, doi:10.1212/01.wnl.0000250326.77323.01 (2007).

85. Schuff, N. *et al.* Selective reduction of N-acetylaspartate in medial temporal and parietal lobes in AD. *Neurology* **58**, 928-935 (2002).

86. Rombouts, S. A. R. B. *et al.* Functional MR Imaging in Alzheimer's Disease during Memory Encoding. *AJNR Am J Neuroradiol* **21**, 1869-1875 (2000).

87. Klunk, W. E. *et al.* Imaging brain amyloid in Alzheimer's disease with Pittsburgh Compound-B. *Annals of Neurology* **55**, 306-319, doi:10.1002/ana.20009 (2004).

88. Wong, D. F. *et al. In vivo* Imaging of Amyloid Deposition in Alzheimer Disease Using the Radioligand 18F-AV-45 (Flobetapir F 18). *Journal of Nuclear Medicine* **51**, 913-920, doi:10.2967/jnumed.109.069088 (2010).

89. Kuntner, C. *et al.* Limitations of Small Animal PET Imaging with [¹⁸F]FDDNP and FDG for Quantitative Studies in a Transgenic Mouse Model of Alzheimer's Disease. *Molecular Imaging and Biology* **11**, 236-240, doi:10.1007/s11307-009-0198-z (2009).

90. Bonte, F. J., Harris, T. S., Hynan, L. S., Bigio, E. H. & White, C. L. I. Tc-99m HMPAO SPECT in the Differential Diagnosis of the Dementias With Histopathologic Confirmation. *Clinical Nuclear Medicine* **31**, 376-378 310.1097/1001.rlu.0000222736.0000281365.0000222763 (2006).

91. Bonte, F. J., Tintner, R., Weiner, M. F., Bigio, E. H. & White, C. L. Brain blood flow in the dementias: SPECT with histopathologic correlation. *Radiology* **186**, 361-365 (1993).

92. Opazo, C. *et al.* Radioiodinated clioquinol as a biomarker for β-amyloid: Zn2+ complexes in Alzheimer's disease. *Aging Cell* **5**, 69-79, doi:10.1111/j.1474-9726.2006.00196.x (2006).

93. Van Heertum, R. L. & Tikofsky, R. S. Positron emission tomography and single-photon emission computed tomography brain imaging in the evaluation of dementia. *Seminars in Nuclear Medicine* **33**, 77-85 (2003).

94. Misgeld, T. & Kerschensteiner, M. In vivo imaging of the diseased nervous system. *Nat Rev Neurosci* **7**, 449-463 (2006).

95. Raymond, S. *et al.* Smart optical probes for near-infrared fluorescence imaging of Alzheimer's disease pathology. *European Journal of Nuclear Medicine and Molecular Imaging* **35**, 93-98, doi:10.1007/s00259-007-0708-7 (2008).

96. Zipfel, W. R. *et al.* Live tissue intrinsic emission microscopy using multiphoton-excited native fluorescence and second harmonic generation. *Proceedings of the National Academy of Sciences* **100**, 7075-7080, doi:10.1073/pnas.0832308100 (2003).

97. Skovronsky, D. M. *et al.* In vivo detection of amyloid plaques in a mouse model of Alzheimer's disease. *Proceedings of the National Academy of Sciences* **97**, 7609-7614, doi:10.1073/pnas.97.13.7609 (2000).

98. Styren, Scot D., Hamilton, R. L., Styren, G. C. & Klunk, W. E. X-34, A Fluorescent Derivative of Congo Red: A Novel Histochemical Stain for Alzheimer's Disease Pathology. *Journal of Histochemistry & Cytochemistry* **48**, 1223-1232, doi:10.1177/002215540004800906 (2000).

99. Kelényi, G. Thioflavin S fluorescent and congo red anisotropic stainings in the histologic demonstration of amyloid. *Acta Neuropathologica* **7**, 336-348, doi:10.1007/bf00688089 (1967).

100. Roney, C. A., Arora, V., Kulkarni, P. V., Antich, P. P. & Bonte, F. J. Nanoparticulate Radiolabelled Quinolines Detect Amyloid Plaques in Mouse Models of Alzheimer's Disease. *International Journal of Alzheimer's Disease*, doi:10.4061/2009/481031 (2009).

101. Vasdev, N., et al. Synthesis and preliminary PET imaging studies of [18F]2-fluoroquinolin-8-ol in transgenic mouse models of Alzheimer's disease. *MedChemComm*, submitted (2011).

102. Ferri, C. P. *et al*. Global prevalence of dementia: a Delphi consensus study. *The Lancet* **366**, 2112-2117 (2005).

103. Ametamey, S. M., Honer, M. & Schubiger, P. A. Molecular Imaging with PET. *Chemical Reviews* **108**, 1501-1516, doi:10.1021/cr0782426 (2008).

104. Wilson, A. A., Jin, L., Garcia, A., DaSilva, J. N. & Houle, S. An admonition when measuring the lipophilicity of radiotracers using counting techniques. *Applied Radiation and Isotopes* **54**, 203-208 (2001).

105. Rikki N, W. Determination of lipophilicity and its use as a predictor of blood–brain barrier penetration of molecular imaging agents. *Molecular Imaging & Biology* **5**, 376-389 (2003).

106. Lee, J.-Y., Cole, T. B., Palmiter, R. D., Suh, S. W. & Koh, J.-Y. Contribution by synaptic zinc to the gender-disparate plaque formation in human Swedish mutant APP transgenic mice. *Proceedings of the National Academy of Sciences* **99**, 7705-7710, doi:10.1073/pnas.092034699 (2002).

107. Watt, N. T., Whitehouse, I. J. & Hooper, N. M. The Role of Zinc in Alzheimer's disease. *International Journal of Alzheimer's Disease* **2011**, doi:10.4061/2011/971021 (2011).

108. Smith, M. A., Harris, P. L. R., Sayre, L. M. & Perry, G. Iron accumulation in Alzheimer disease is a source of redox-generated free radicals. *Proceedings of the National Academy of Sciences* **94**, 9866-9868 (1997).

109. Butterfield, D. A., Reed, T., Newman, S. F. & Sultana, R. Roles of amyloid β-peptide-associated oxidative stress and brain protein modifications in the pathogenesis of Alzheimer's disease and mild cognitive impairment. *Free Radical Biology and Medicine* **43**, 658-677 (2007).

110. Wong, Y. O., Miranda, P. & Rosenberg, E. Metal coordination and selectivity with oxine ligands bound to silica polyamine composites. *Journal of Applied Polymer Science* **115**, 2855-2864, doi:10.1002/app.31229 (2010).

111. Jago, J., Wilson, P. E. & Lee, B. M. Determination of sub-microgram amounts of cobalt in plants and animal tissues by extraction and atomic-absorption spectroscopy. *Analyst* **96**, 349-353 (1971).

112. Simmons, W. J. Determination of low concentrations of cobalt in plant material by atomic absorption spectrophotometry. *Analytical Chemistry* **45**, 1947-1949, doi:10.1021/ac60333a033 (1973).

113. Bratzel, M. P., Aaron, J. J., Winefordner, J. D., Schulman, S. G. & Gershon, H. Investigation of excited singlet state properties of 8-hydroxyquinoline and its derivatives by fluorescence spectrometry. *Analytical Chemistry* **44**, 1240-1245, doi:10.1021/ac60315a020 (1972).

114. Soroka, K., Vithanage, R. S., Phillips, D. A., Walker, B. & Dasgupta, P. K. Fluorescence properties of metal complexes of 8-hydroxyquinoline-5-sulfonic acid and chromatographic applications. *Analytical Chemistry* **59**, 629-636, doi:10.1021/ac00131a019 (1987).

115. Frederickson, C. J., Kasarskis, E. J., Ringo, D. & Frederickson, R. E. A quinoline fluorescence method for visualizing and assaying the histochemically reactive zinc (bouton zinc) in the brain. *Journal of Neuroscience Methods* **20**, 91-103 (1987).

116. Farruggia, G. *et al.* 8-Hydroxyquinoline Derivatives as Fluorescent Sensors for Magnesium in Living Cells. *Journal of the American Chemical Society* **128**, 344-350, doi:10.1021/ja056523u (2005).

117. Jiang, P. & Guo, Z. Fluorescent detection of zinc in biological systems: recent development on the design of chemosensors and biosensors. *Coordination Chemistry Reviews* **248**, 205-229 (2004).

118. Feranchak, A. P. *et al.* Initiation of Purinergic Signaling by Exocytosis of ATP-containing Vesicles in Liver Epithelium. *Journal of Biological Chemistry* **285**, 8138-8147, doi:10.1074/jbc.M109.065482 (2010).

119. Fahrni, C. J. & O'Halloran, T. V. Aqueous Coordination Chemistry of Quinoline-Based Fluorescence Probes for the Biological Chemistry of Zinc. *Journal of the American Chemical Society* **121**, 11448-11458, doi:10.1021/ja992709f (1999).

120. Ribou, A. C., Vigo, J., Viallet, P. & Salmon, J. M. Interaction of a protein, BSA, and a fluorescent probe, Mag-Indo-1, influence of EDTA and calcium on the equilibrium. *Biophysical Chemistry* **81**, 179-189 (1999).

121. Nyborg, J. K. & Peersen, O. B. That zincing feeling: the effects of EDTA on the behaviour of zinc-binding transcriptional regulators. *Biochem. J.* **381**, e3-e4 (2004).

122. Qu, B., Boyer, P. J., Johnston, S. A., Hynan, L. S. & Rosenberg, R. N. Aβ42 gene vaccination reduces brain amyloid plaque burden in transgenic mice. *Journal of the Neurological Sciences* **244**, 151-158 (2006).

123. Wang, H., Wang, W.-S. & Zhang, H.-S. A spectrofluorimetric method for cysteine and glutathione using the fluorescence system of Zn(II)-8-hydroxyquinoline-5-sulphonic acid complex. *Spectrochimica Acta Part A: Molecular and Biomolecular Spectroscopy* **57**, 2403-2407 (2001).

124. Mehata, M. S. FLUORESCENCE CHARACTERISTICS OF 2-HYDROXYQUINOLINE IN VARIOUS SOLVENTS. *J. Instrum. Soc. India* **35**, 249-256 (2005).

125. Weng, Y., Chen, Z., Wang, F., Xue, L. & Jiang, H. High sensitive determination of zinc with novel water-soluble small molecular fluorescent sensor. *Analytica Chimica Acta* **647**, 215-218 (2009).

126. Choi, S. R. *et al.* Preclinical Properties of 18F-AV-45: A PET Agent for Aβ Plaques in the Brain. *Journal of Nuclear Medicine* **50**, 1887-1894, doi:10.2967/jnumed.109.065284 (2009).

127. Loening AM, G. S. AMIDE: a free software tool for multimodality medical image analysis. *Mol Imaging* **2**, 131-137 (2003).

128. MacKenzie-Graham, A. *et al.* The informatics of a C57BL/6J mouse brain atlas. *Neuroinformatics* **1**, 397-410, doi:10.1385/ni:1:4:397 (2003).

129. Rey, N. L. *et al.* Locus coeruleus degeneration exacerbates olfactory deficits in APP/PS1 transgenic mice. *Neurobiology of Aging* In Press, Corrected Proof.

130. Stoltenberg, M. *et al.* Amyloid plaques arise from zinc-enriched cortical layers in APP/PS1 transgenic mice and are paradoxically enlarged with dietary zinc deficiency. *Neuroscience* **150**, 357-369 (2007).

131. Yang, X., Dai, G., Li, G. & Yang, E. Coenzyme Q10 Reduces β-Amyloid Plaque in an APP/PS1 Transgenic Mouse Model of Alzheimer's Disease. *Journal of Molecular Neuroscience* **41**, 110-113, doi:10.1007/s12031-009-9297-1 (2010).

132. Li-hong Z, D. Y., Xin W, Wei Z, Ming R, Zhan-you W. Distribution of zinc ions and zinc transporter-6 in the APP/PS1 transgenic mouse cerebellum. *FuDan University journal of Medical Sciences* **36**, 65-69 (2009).

133. Kung, M.-P., Zhuang, Z.-P., Hou, C. & Kung, H. Development and evaluation of iodinated tracers targeting amyloid plaques for SPECT imaging. *Journal of Molecular Neuroscience* **24**, 49-53, doi:10.1385/jmn:24:1:049 (2004).

134. Phelps, ME. PET: molecular imaging and its biological applications. (Sprenger-Verlag New York, Inc, 2004).

135. Di Vaira, M. *et al.* Clioquinol, a Drug for Alzheimer's Disease Specifically Interfering with Brain Metal Metabolism: Structural Characterization of Its Zinc(II) and Copper(II) Complexes. *Inorganic Chemistry* **43**, 3795-3797, doi:10.1021/ic0494051 (2004).

136. Sekler, I. *et al.* Distribution of the zinc transporter ZnT-1 in comparison with chelatable zinc in the mouse brain. *The Journal of Comparative Neurology* **447**, 201-209, doi:10.1002/cne.10224 (2002).

137. Wang, J., Tanila, H., Puoliväli, J., Kadish, I. & Groen, T. v. Gender differences in the amount and deposition of amyloid[beta] in APPswe and PS1 double transgenic mice. *Neurobiology of Disease* **14**, 318-327 (2003).

138. Budimir, A. *et al.* Hydroxyquinoline based binders: Promising ligands for chelatotherapy? *Journal of Inorganic Biochemistry* **105**, 490-496 (2011).

139. Kulkarni, P. *et al.* PET imaging of Alzheimer's disease (AD) transgenic mice with a F-18 labeled hydroxy quinoline derivative. *J NUCL MED MEETING ABSTRACTS* **51**, 1746 (2010).

140. DeGrado, T. R., Reiman, R. E., Price, D. T., Wang, S. & Coleman, R. E. Pharmacokinetics and Radiation Dosimetry of 18F-Fluorocholine. *Journal of Nuclear Medicine* **43**, 92-96 (2002).

141. Tang, G., Wang, M., Tang, X., Luo, L. & Gan, M. Pharmacokinetics and radiation dosimetry estimation of O-(2-[18F]fluoroethyl)--tyrosine as oncologic PET tracer. *Applied Radiation and Isotopes* **58**, 219-225 (2003).

142. Brown, W. D. *et al.* Fluorine-18-Fluoro-L-DOPA Dosimetry with Carbidopa Pretreatment. *Journal of Nuclear Medicine* **39**, 1884-1891 (1998).

143. Mejia, A. A. *et al.* Estimation of Absorbed Doses in Humans Due to Intravenous Administration of Fluorine-18-Fluorodeoxyglucose in PET Studies. *Journal of Nuclear Medicine* **32**, 699-706 (1991).

144. Snyder W.S. , F. M. R., Warner G.G. , Watson S. B. . MIRD Pamphlet #11: S, Absorbed Dose per Unit Cumulated Activity for Selected Radionuclides and Organs. *Society of Nuclear Medicine* (1975).

145. Bouchet, L. G. *et al.* MIRD Pamphlet No. 15: Radionuclide S Values in a Revised Dosimetrie Model of the Adult Head and Brain. *Journal of Nuclear Medicine* **40**, 62S-101S (1999).

146. STANFORD DOSIMETRY, L. <http://www.doseinfo-radar.com/>

147. Coffey Jack L. , C. M., Warner Gordon G. . MIRD Pamphlet #13: Specific Absorbed Fractions for Photon Sources Uniformly Distributed in the Heart Chambers and Heart Wall of Heterogeneous Phantom. *J Nucl Med* **22**, 65-71 (1981).

148. Weber David A, E. K. F., Dillman L. Thomas, Ryman Jeffrey C. *MIRD: Radionuclide Data and Decay Schemes*. (The Society of Nuclear Medicine, Inc., 1989).

149. Loevinger Robert, B. T. F., Watson Evelyn E. *MIRD Primer for Absorbed Dose Calculations* (The society of Nuclear Medicine, Inc, 1988).

150. Snyder WS , F. M. R., Warner GG , Fisher HL MIRD Pamphlet #5 Revised: Estimates of Absorbed Fractions for Monoenergetic Photon

Sources Uniformly Distributed in Various Organs of a Heterogeneous Phantom. *J Nucl Med* (1969).

151. Khalil, M.M. Basic sciences of nuclear medicine. (Springer-Verlag, 2011).

152. CFR - Code of Federal Regulations Title 21, <http://www.accessdata.fda.gov/scripts/cdrh/cfdocs/cfcfr/CFRSearch.cfm?fr=361.1>

153. A Summary of Radiation Dose Guidelines and Limits Applicable to Human Subjects in Research Studies, http://www.ehs.umaryland.edu/Rad/pdf/A%20Summary%20of%20Radiation%20Dose%20Guidelines%20and%20Limits%20Applicable%20to%20Human%20Subjects%20in%20Research%20Studies.pdf